AEROSOL FORMATION IN CO_2 CAPTURE PLANTS - MOLECULAR DYNAMICS SIMULATION

Ulan Mansurov, Bachelor of Engineering in Chemical Engineering

Submitted in fulfilment of the requirements
for the degree of Masters of Science
in Chemical Engineering

School of Engineering
Department of Chemical Engineering
Nazarbayev University

53 Kabanbay Batyr Avenue,
Astana, Kazakhstan, 010000

Supervisors: Mehdi Amouei Torkmahalleh & Dhawal Shah

January, 2018

DECLARATION

I hereby, declare that this manuscript, entitled *"Aerosol formation in CO_2 capture plants - Molecular Dynamics Simulation",* is the result of my own work except for quotations and citations which have been duly acknowledged. I also declare that, to the best of my knowledge and belief, it has not been previously or concurrently submitted, in whole or in part, for any other degree or diploma at Nazarbayev University or any other national or international institution.

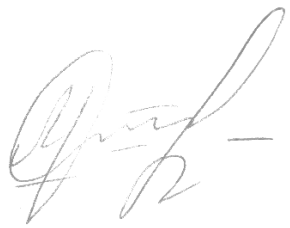

Name: Ulan Mansurov

Date: 25.01.2018

Abstract

Carbon dioxide capture is becoming a major concern not only from the perspective of traditional sour gas sweetening but also because of adverse effects of CO_2 on climate change. The most conventional method to eliminate CO_2 is carried out in a post-combustion CO_2 capture (PCCC) column using aqueous monoethanolamine (MEA) as a solvent. Numerous reports have manifested significant amount of solvent losses due to formation of aerosols in PCCC columns. This research provides insights into formation mechanisms of aerosols or particulate matter (PM) at a molecular level by emphasizing interaction parameters between participating components. Molecular dynamics (MD) simulations were performed using GROMACS software. Five different systems under ordinary PCCC conditions were considered each of which has unique configuration of components. MD simulations revealed evolution and development of molecular clusters that formed PM which consisted of all gaseous MEA, SO_2, major portion of CO_2, and water vapor. Furthermore, quantitative analysis of the molecular clusters was carried out in terms of CO_2 molecules. Nucleation rates of PM were in the order of 10^{-30} $cm^{-3}s^{-1}$. Also, formed aerosol particles were structurally examined using radial distribution functions (RDF) and determining pair potentials between the molecules. It was found that MEA in vapor phase contributes to PM formation. Furthermore, strong attraction potential between water and CO_2 and MEA imply that the

presence of water in vapor phase might be one of the key factors that forms and sustains PM. Taken together, the results are first of the efforts to understand PM (aerosol) formation in a typical PCCC column based on molecular simulations, and based on the findings of the study, certain practical suggestions were offered to avoid formation of PM.

Acknowledgments

Firstly, I would like to express my uttermost gratitude towards my supervisors Dhawal Shah and Mehdi Torkmahalleh. It has been their supervision and direction throughout the duration of my studies which has allowed me to successfully complete this Master's thesis. I am appreciative for all the hours of discussion they have offered me, and privileges they have kindly provided to me.

Secondly, I would like to show my indebtedness to the Nazarbayev University and its community.

Thirdly, I would like to thank my family and my relatives for their constant support.

Table of Contents

Abstract **1**
Acknowledgments **3**
List of Abbreviations **5**
List of Figures **6**
List of Tables **7**
Chapter 1 – Introduction 8
Chapter 2 – Literature Review 14
2.1 Reactions between CO_2 and MEA
2.2 Molecular modelling of CO_2 and MEA
2.3 Identification and modelling of PM
Chapter 3 – Materials and Methods 29
3.1 Design of the simulation system
3.2 Test for supersaturation
3.3 Simulation methodology
3.4 Validation of forcefield parameters
Chapter 4 – Results and Discussion 38
4.1 Visual analysis
4.2 Quantitative analysis of the clusters
4.2.1 Nucleation rate
4.3 Structural analysis of the clusters
Chapter 5 – Conclusion 60
Reference list **63**
Appendices **67**

List of Abbreviations

AIMD – Ab initio molecular dynamics, a DFT-based accurate molecular dynamics tool related to small systems
ATB – Automated Topology Builder
DEA – Diethanolamine
DFT – Density functional theory
ELECNRTL – Electrolyte Non-random Two Liquid (Thermodynamic model)
FTIR - Fourier-Transform Infrared Spectroscopy
G (mg) – Gram (milligram)
GROMACS - Groningen Machine for Chemical Simulations, a molecular dynamics simulation package
H-bond – Hydrogen bond
LAMMPS - Large-scale atomic/ molecular massively parallel simulator, a molecular dynamics simulation software
LINCS – Linear Constraint (solver, algorithm)
LJ - Lennard-Jones (potential)
MD – Molecular Dynamics
MDEA - Methyl diethanolamine
MEA – Monoethanolamine
MMR - Nuclear Magnetic Resonance
Mol% - Percentage in terms of mole
NRTL - Non-random Two Liquid (Thermodynamic model)
NVT – a MD ensemble, in which number of molecules, volume, and temperature are held constant
PCCC – Post-combustion CO_2 capture
PFR – Plug flow reactor
PM – Particulate matter
PZ – Piperazine (solvent for CO_2 capture)
QM – Quantum Mechanics, a fundamental physics theory
RDF – Radial Distribution Function
S (ps, ns) – Second (picosecond, nanosecond)
TEA - Triethanolamine
VMD – Visual Molecular Dynamics, a tool for visualization of molecular simulations
Wt% - Percentage in terms of weight
[atom or molecule] – Concentration of that atom or molecule

List of Figures

Figure 2.1: Light dispersion dependence on time for the mixture of carbon dioxide to argon 1:10^4 21
Figure 2.2: Schematic representation of two absorbers simulated in Aspen Plus 24
Figure 2.3: Diameter of the aerosol drops against height of the column 26
Figure 2.4: Aspen Plus flowsheet to model aerosol-based amine emissions 26
Figure 3.1: Aspen Plus flowsheet to calculate saturation values for the systems 32
Figure 4.1: Snapshots from the simulation with 1 MEA and 1081 CO_2, system I 39
Figure 4.2: Snapshot from the simulation with 10 MEA and 1081 CO_2, system II 40
Figure 4.3: Snapshot from the simulation with 25 MEA and 1081 CO_2, system III 41
Figure 4.4: Snapshot from the simulation with 1 MEA, 1081 CO_2, water, nitrogen, and oxygen molecules, system IV 43
Figure 4.5: Snapshots from the simulation of system V containing MEA, CO_2, water, nitrogen, oxygen, and sulfur dioxide molecules, system V 44
Figure 4.6: The number of clusters decreases forming larger clusters for all the systems, except system I, with time during the (a) NVT ensemble (b) 10 ns MD simulation run ... 46
Figure 4.7: Number of molecules in the largest cluster increasing with time during the (a) NVT ensemble (b) 10 ns MD run 49
Figure 4.8: Number of molecules per unit time for systems II and III 50
Figure 4.9: Number of molecules per unit time for system V 51
Figure 4.10: Radial distribution functions between the carbon atoms of CO_2 molecules for all five systems 54
Figure 4.11: RDF between carbon molecules of CO_2 and MEA 54
Figure 4.12: Interaction energy between MEA and CO_2 for the five systems 55
Figure 4.13: Interaction energy between CO_2 molecules 56
Figure 4.14: Hydrogen bonds between water and MEA in system IV 58
Figure 4.15: RDF between carbon atom of CO_2 and oxygen atom of water 59

List of Tables

Table 2.1: Specifications of flue inlet gas to the absorption column 27

Table 2.2: Reactions that occur during CO_2 capture 28

Table 3.1: The components present and their concentrations in a typical PCCC in the gas phase at 60 ^oC and 1 bar 29

Table 3.2: The number of molecules of individual components chosen to simulate different systems to systematically explore the aerosol formation in typical PCCC 31

Table 3.3: Results of phase equilibrium pressures and supersaturation values 33

Table 3.4: Partial charges and other interaction parameters for CO_2 as obtained from ATB server, Cygan et al., and Moosavi et al. 36

Table 3.5: Average density and self-diffusion coefficient values for MEA and CO_2 as obtained from three different sets of force field parameters 37

Table 4.1: Energy analysis results for system IV 57

Chapter 1 - Introduction

The global average temperature on the Earth has risen for 0.8^{o}C in the last hundred years [1]. According to climate science, 2^{o}C increase in the temperature could prompt destructive environmental consequences [2]. Negative impacts of the climate change have already been observed throughout the planet [3-5]. Global warming and its consequences have been linked to the growing level of greenhouse gases in the atmosphere [6-8]. According to the United States Environmental Protection Agency, 77% of global greenhouse gas emissions is carbon dioxide [9].

For the reasons stated above, increasing level of carbon dioxide in the atmosphere has been a significant issue due to its unequivocal influence on the climate change of the planet. Its level in the atmosphere has reached 406.94 ppm in September 2017, while before industrial civilization its historical average level was about 250 ppm [10]. Natural equilibrium of carbon dioxide has been deteriorated by anthropogenic activities, and particularly it is caused by burning of fossil fuels [11]. Combustion of carbon alone results in 24 gigatons of CO_2 emission every year [11]. In 2014 USA produced 82.78% of its energy by fossil fuels, whereas Kazakhstan relies on fossil fuels by 99.17% [12]. As fossil fuels are going to be the primary source of energy for most of the countries, appropriate mitigation measures should be taken to decrease or at least sustain the current level of CO_2 in the atmosphere. Moreover, due to its sour nature,

excess level of CO_2 in a gas stream has been linked to pipe corrosion, catalyst deactivation, and decrease in the gas heating value [13]. In this regard, carbon capture method has been proposed as an attractive option to decrease the concentrations of CO_2 [14]. Carbon dioxide capture technology could reduce CO_2 emissions from fossil fuels by 80% to 90% [15]. This amount of carbon dioxide is inhaled by approximately 62 million trees in 10 years [15].

Carbon capture is being implemented industrially. Initially, CO_2 capture was carried out not from ecological concerns, but to use the captured gas for enhanced oil recovery [16]. First plants with carbon capture technology started operating in USA in 1980s [16]. Up to April of the last year, there have been 14 operating facilities with the carbon capture process implemented [17].

Generally, carbon dioxide capture technology can be applied to various systems. Accordingly, carbon capture system is divided into three categories: post-combustion, pre-combustion, and oxyfuel [18]. These are sometimes called as ‘flue gas’, ‘hydrogen route’, and ‘denitrogenation’, respectively [18]. Among these alternatives, post-combustion CO_2 capture is the most advanced [18]. Also, unlike others, it can be applied to the existing facilities without interrupting the process [18].

The most widespread and effective post-combustion CO_2 capture method is by means of chemical absorption using MEA as a solvent [19, 20]. MEA is an alkanolamine, organic polar compound that consist of ethyl, alcohol, and amine group and has a chemical formula NH_2-C_2H_4-OH [21]. Conventionally, 30 wt%

(or 10 mol%) aqueous MEA is implemented in the industry [22-24]. This configuration is a tradeoff between numerous factors. High concentration of MEA would lead to high viscosity and corrosivity, whereas its low concentration result in low absorption capacity and high energy intensity of the process due to high water content [25]. Generally, amines have been widely used for acid gases removal during last six decades [26]. They are well known for their reversible reactions with CO_2 [26]. This feature enables to use amines for multiple CO_2 scrubbing cycles. Also, MEA is preferred because of its low cost, availability, high reactivity, moderate thermal decomposition rate, low molecular mass, and high absorption capacity [13]. Furthermore, it was claimed that MEA is the most efficient solvent to capture CO_2 from a low-pressure gas stream [25]. Nevertheless, disadvantages of absorption of CO_2 by amines are substantial solvent loss, high energy requirement, and decomposition of the solvent to detrimental and corrosive products [19, 22]. Other methods of carbon dioxide capture are: membrane separation, cryogenic separation, and physical adsorption using molecular sieves [16]. However, they are believed to be expensive compared to the chemical absorption method [16].

As it was stated earlier, one of the main drawbacks of CO_2 capture using MEA is the solvent loss. It was estimated that during chemical absorption of CO_2 with 30 wt% aqueous MEA, 15.6 kg of the solvent is lost per ton of CO_2 captured [27]. Apart from obvious economic loss, it poses environmental threats.

Degradation products of amines, such as nitrosamines are known to be carcinogenic [28].

It has been accepted that amine emissions are predominantly driven by volatility of the solvents. Amine losses associated with their volatility are quantified in the range between 12 mg and 147 mg per normal m^3 of treated gas stream [29]. Conventionally, water washing sections, demisters, and cyclones are applied to mitigate these losses. However, recently it was pointed out that particulates emerging or existing in the absorption columns can drastically increase amine emissions [29]. They have contributed to solvent loss in the amount from 200 mg to 1100 mg per m^3 of the gas [29]. Recent experiments and field studies also confirm the loss of MEA in the form of PM (aerosols) in PCCC mini plants [30-32]. The two terms, PM and aerosol, have been used interchangeably in chemical engineering literature. Particulate matter is defined as “a complex mixture of extremely small particles (solids or liquid droplets), made up of acids, organic chemicals, metals, and soil or dust particles” [33]. The term ‘aerosol’ refers to the particles and the surrounding gas collectively [34-36]. As gas phase already exists in PCCC column, using the term PM is more relevant. Traditional methods to reduce solvent emissions were inefficient to remove particles with sizes less than 5 μm [29]. Pilot plant observations made by Kamijo [37], van der Gjip et al. [38], and Kolderup et al. [39] suggested that amine emission can be effectively tackled with addressing PM (aerosol) formation issue.

It has been suggested that PM development pertains to the degree of saturation, which is defined as [40]:

$$S = \left(\frac{Pc(T,y)}{Pcs\ (T,y)}\right) \qquad \text{(E1)}$$

where, P_c is the partial pressure of a condensable gaseous component at temperature T, P_{cs} is the partial pressure of the condensable component at phase equilibrium (saturation pressure). When equation E1 shows supersaturation for a given system with one condensable component (S>1), then the precondition for PM formation through homogeneous nucleation is met [40]. For systems with several condensing species, their individual saturation value need not necessarily exceed 1 for nucleation to take place [40]. Moreover, for systems that contain more than one condensable component, Schaber [41] was the first who extended equation E1 as following:

$$S = (\sum Pc(T, y_1, y_2, \ldots))/(\sum Pcs\ (T, y_1, y_2 \ldots)) \qquad \text{(E2)}$$

Nevertheless, the extension of equation E1 to equation E2 does not have strong scientific support and may not be sufficient to observe supersaturation in a mixture with several condensing components.

Despite few attempts made in studying aerosols, hitherto prerequisites, driving forces and mechanism of formation of aerosols remain unclear [42]. There is a need for an extensive study that would embrace computer simulation, analytical approach, and empirical affirmation. Thorough comprehension of aerosol emergence through PM formation would enable to implement effective

countermeasures against emissions in form of particulate matter and make CO_2 capture economically feasible and environmentally safe.

This pioneer research aims to provide understanding of formation, evolution and development of particulate matter using molecular dynamics simulation tools. Unlike classical approach, molecular dynamics simulations can give insights to the chemical processes at a molecular level [43]. Five different systems in vapor phase with various configurations of MEA, CO_2, water, air components, and SO_2 will be under consideration. GROMACS simulation package along with VMD visualization tool will be used to reach the objectives. Appropriate force field parameters will be selected, validated, and employed in the simulations. Preconditions of each system will be determined using process simulator ASPEN PLUS. The systems with high value of saturation ratio are likely to witness formation of distinct molecular clusters. These clusters will be studied in terms of their quantity and structure. Nucleation rate of clusters, thus PM, will be calculated. Also, the driving and sustaining forces of formed clusters will be identified using RDF and interaction energy analysis.

Chapter 2 - Literature Review

2.1 REACTIONS BETWEEN CO_2 AND MEA

The whole process of CO_2 absorption by MEA is based on reactivity of the molecules with each other. MEA - CO_2 reaction has been an object of several studies. Bottinger et al. [44] used online NMR spectroscopy to discover product species of the reaction between aqueous solution of MEA (30 wt% and 20 wt%) and CO_2 under various pressures and in temperature ranges between 20^{o}C and 80^{o}C. Two scenarios were considered: CO_2 gas at low and high pressures, which were represented as CO_2 to MEA molar ratio. Up to CO_2 to MEA molar ratio of 0.5, MEA molecules were consumed quickly and almost vanished when the CO_2 to MEA ratio attained to 0.5. On the other hand, concentrations of $MEAH^+$ and $MEACOO^-$, products of the reaction, increased in the same manner. When CO_2 to MEA relation surpassed 0.5, which indicated higher pressure of CO_2, concentration of $MEACOO^-$ started to decrease rapidly and bicarbonate emerged in considerable amount. Han et al. [45] advanced further applying molecular simulations in a strive to understand CO_2 – MEA reaction mechanism. They performed MD simulations of CO_2 and MEA in liquid phase in ratios of former to the latter 0.5 and 1 at 313 K. The authors followed previous work by Bottinger et al. and proposed two reaction schemes depending on low and high CO_2 pressures. In first case, the following overall reaction scheme was suggested:

$$2MEA + CO_2 \leftrightarrow MEAH^+ + MEACOO^- \quad (R1)$$

And authors proposed and performed quantum chemical calculations on two ways of reaching the overall reaction scheme (R1). The first route is given below:

$$MEA + CO_2 \leftrightarrow MEACOOH \quad (R2)$$

$$MEACOOH + MEA \leftrightarrow MEAH^+ + MEACOO^- \quad (R3)$$

The second proposed reaction pathway involves a zwitterion intermediate product and is presented below:

$$MEA + CO_2 \leftrightarrow MEA^+COO^- \quad (R4)$$

$$MEA^+COO^- + MEA \leftrightarrow MEAH^+ + MEACOO^- \quad (R5)$$

It was found that attachment of CO_2 to MEA was achieved through formation of a weak C-N bond and loosening of the N-H bonding [45, 46]. Also, intramolecular and intermolecular hydrogen bonding reciprocal actions influenced proton acquiring capability of MEA and formed carbamate [46]. Presuming that proton transfers mainly take place via water bridges, a strong dependence of the whole reaction on water molecules disposition around zwitterion has been established [46]. Caplow in 1968 [47] and then Danckwertz in 1979 [48] were among the first who put forward that reaction between CO_2 and monoethanolamine almost certainly follows a zwitterion mechanism. Another study conducted by Shim et al. [49] also revealed that the zwitterion mechanism is consistent with MEA as a proton acceptor. The latter reaction

route (R5) was calculated to have very low energy barriers and stated to be the most convenient in terms of energy [45].

Scientific community was skeptical about reactions (R4) and (R5) because experimental inspections had not detected zwitterions [24]. Quite earlier a group of researchers led by Xie [24] also explored MEA – CO_2 reaction with help of transition state calculations where effective solvent model was implemented. Mean force calculations were conducted utilizing B3LYP/ B1 QM/MM MD simulations. The study confirmed that MEA - CO_2 reaction undergoes a two-step pathway entailing a zwitterion intermediate (reactions (R4) and (R5)). Generation of the intermediate was pointed to be a rate-determining step. The activation energy for the slowest step was computed to be 12.0 and 11.3 kcal/mol, whereas experimental value is around 12.4 kcal/mol. Empirical attempts to identify reaction order of MEA unanimously yield values around one. Completing step of MEA – CO_2 reaction mechanism was found to be acid-base reaction between the intermediate product and MEA (reaction (R5)). Reaction rate coefficient k and effective reaction order matched with experimental values. The authors found that intermediate product equilibrium concentration was about 10 - 11 mole/liter, which explains why zwitterions were not experimentally observed before.

In case of high CO_2 pressure, also referring to the research of Bottinger et al. [44], following reaction way was proffered [45]:

$$MEA + CO_2 + H_2O \leftrightarrows MEAH^+ + HCO^{-3} \qquad (R6)$$

Noticeably, unlike during low pressure of CO_2 water takes part in reaction and MEA behaves as an alkali [45].

2.2 MOLECULAR MODELLING OF MEA AND CO_2

Available literature presents several attempts to model MEA and CO_2 using molecular dynamics tools. Button et al. [50] implemented a mix of amine and alcohol forcefields to model MEA. However, obtained characteristic values were not validated with experimental data. Later, Alejandre et al. [21] proposed a force field that yields acceptably accurate values of density, critical point, and surface tension. Nevertheless, it was not mentioned whether this model can be applied to model *vapor* phases. Another effort was made by Lopez-Rendon et al. [51] . They provided force field parameters to simulate *liquid* MEA, DEA, MDEA, and TEA. The employed forcefield results, particularly, calculated dipole moments, excess molar volumes, and densities agreed with the experimental data. However, the forcefield is applicable only to pure liquids [51]. Similar work has been done by Han et al. [23] . The authors proposed to use pure liquid MEA but did not report the ways to handle high viscosity of MEA in an absorption column. A research group led by Da Silva et al. [52] advanced further to develop force field parameters that would enable adequate simulation of pure MEA, 30 wt% aqueous MEA, and MEA with CO_2. They developed three force field models: two for MEA and one for CO_2. For simulation, they used AMBER package and implemented NPT (1 bar, 298 and

333K) ensemble for equilibration [52]. Five systems were under consideration [52]:

1. 512 molecules of MEA
2. 52 molecules of MEA and 460 H_2O molecules
3. 1 CO_2, 52 MEA, and 460 water molecules
4. 1 MEA and 511 water molecules
5. 512 water molecules

Reactions were neglected in each system. Force field results, namely densities, excess molar volumes, dielectric constants, and dipole moments were validated experimentally. As MEA represents a plain organic molecule that readily forms intramolecular H-bonds, authors found that in pure MEA predominant H-bonding is between oxygen and hydrogen bounded to nitrogen. In 30 wt% aqueous MEA solution intermolecular H-bonding (such as N-H(N) and N-H(O)) strengths are suppressed and this factor determines its conformational arrangement. In more details, RDF graphs revealed that interaction between hydrogen in alcohol group of MEA and oxygen of water is of high frequency. Consecutively, MEA attaches to water molecule through hydroxyl group. Also, it was suggested that MEA, CO_2, and second MEA (to accept proton (acting as a base)) are in ease availability and finely lined up to react with each other. They also discovered that O-C-C-N dihedral of MEA in its pure and aqueous conditions was usually disposed in gauche conformation. Unfortunately, MEA in gas phase was only studied to identify conformers.

Interestingly, RDF profiles obtained by da Silva et al. [52] demonstrated that water molecules enhance attraction between carbon atoms of MEA. From this important finding it can be inferred that water molecules contribute to coalescence of carbon atoms. Nevertheless, authors underestimate this uncovering by concluding that this property is not so strong as to predict any substantial aggregation of MEA molecules.

2.3 IDENTIFICATION AND MODELLING OF PM

PM formation in a PCCC column starts with creation and development of small molecular clusters. In this regard, critical cluster size and nucleation rate are crucial parameters. Critical cluster size is a characteristic size of an assembly of molecules surpassing of which leads to further growing of the cluster due to a net reduction in its free energy [43]. Nucleation rate is the growth rate of assembling clusters over and above the critical cluster size per volume and time [43]. There are two types of nucleation. Homogeneous nucleation takes place spontaneously forming a new interface at a new phase boundary [53, 54]. Heterogeneous nucleation, on the contrary, occurs on a pre-existing surface [53, 54].

The published studies principally focus on crystal CO_2 clusters overlooking intermediate liquid phase. Disselkamp and Ewing [55] investigated formation of large CO_2 clusters using infrared spectroscopy and light scattering. The cluster formation took place in a cryogenic cell at 77 K in an argon environment. Although the authors link formation of clusters to supersaturation,

its calculation methods were not reported. Disselkamp and Ewing conducted laser light scattering test and witnessed dramatic decrease in light transmittance for the 0.01% mixture of CO_2 to argon after 60 s in the cell (see figure 2.1). They ascribed it to the formation of *spherical* clusters (particulate matter). Infrared spectroscopy results also endorsed this finding. Number of CO_2 molecules in the clusters ranged from 10^8 to 10^9. Their molecular adjustment resembled crystalline structure. The authors developed a set of equations that combine the results of infrared spectroscopy and laser light dissipation to estimate radius of formed clusters. Besides, they criticize Mie and exciton model to describe spectroscopy results. Referring to figure 2.1, after some time light transmittance starts to increase gradually, which implies dissipation of the clusters. The authors provided two ways of disappearance of the clusters: by diffusion and by sedimentation. They conclude that the process is predominantly driven by sedimentation. Nevertheless, complete conclusion regarding formation of spherical clusters in this work could not be inferred.

Figure 2.1: Light dispersion dependence on time for the mixture of carbon dioxide to argon 1:10^4. Adopted from Disselkamp and Ewing [55].

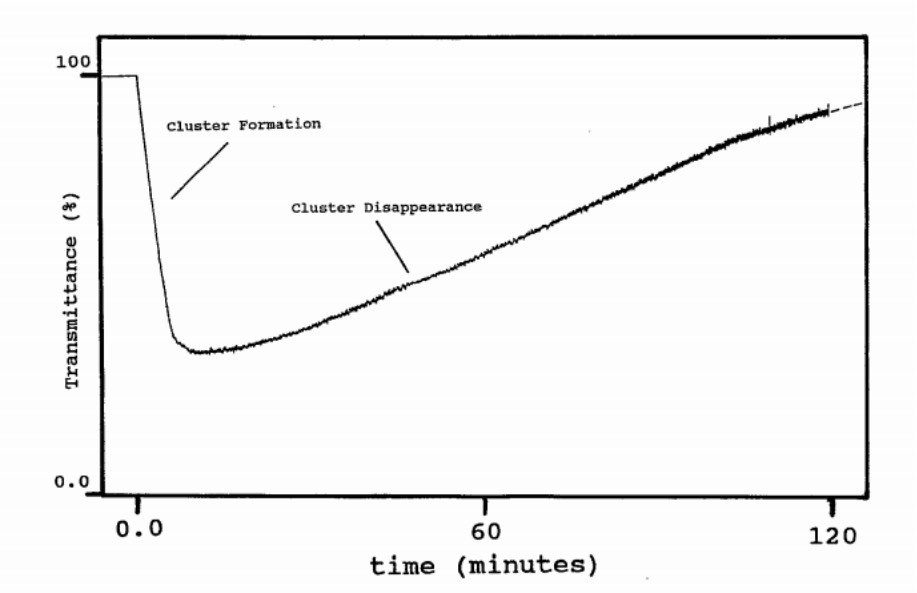

It was already mentioned earlier that due to recent emergence of the issue, PM (aerosol phase) formation and development during PCCC has been an object of only few studies. In their article a team of researchers headed by Mertens [42] used Fourier Transform Infra-Red (FTIR) spectroscopy in order to identify ammonia emissions and mist (aerosol) formations of a gas stream in a CO_2 absorber column. Employed solvent was MEA. Mertens et al. [42] used heated sample of gas at temperature of 180^{o}C to avoid unnecessary condensation and loss of the solvent. As a result, the authors found a direct proportionality between MEA emission and metal ions present in the gas. This finding has been confirmed in a pilot plant testing. FTIR results and field tests also revealed that MEA emission increases over time. According to the team, this can be explained by aerosol formation in the absorption column. The authors also suggested that aerosol formation is largely dependent on the presence of trace materials, such

as sulfur compounds, fly ash, and other metals. Another investigation led by Khakharia [29] also found a relationship between MEA emission and sulfuric acid and soot present in flue gas stream. Sulfuric acid concentrations of 10^8 particles per cm^3 caused the solvent loss of about 600 - 1100 mg per normal m^3 of treated flue gas. This finding suggests that sulfuric acid while being present serves as nucleation center for aerosol formation. The authors also demonstrated that increasing CO_2 flow in the flue gas results in drastic increase in MEA emission and based on this finding predicted that CO_2 itself may have much more effect on aerosol formation than it thought to have. In another field test conducted by de Cazenove et al. [56] it was found that PM mostly comprised of water molecules. Sizes of the particles were identified ranging from 0.43 μm to 4.7 μm. In another recent experiment PM sizes were quantified in the range between 0.3 μm and 17.5 μm [57].

Furthermore, few studies have been carried out to model aerosols. Fulk and Rochelle [28] developed aerosol model using Aspen Plus software. PM was assumed of *spherical* shape, and its transport model was scripted in MATLAB. Piperazine (PZ) was employed as a solvent. It is a cyclic amine that has a feasible CO_2 absorption capacity. At equilibrium conditions, carbon dioxide and piperazine equilibrium partial pressures are given as follows [28] :

$$\text{Ln}\ (P_{CO2}) = [35.3 - 11054/T^L - 18.9a^2 + 4958a/T^L + 10163a^2/T^L] \quad \text{(E3)}$$

$$\text{Ln}\ (P_{PZ}/x_{PZ}) = [-123 - 21.6\ lnT^L - 20.2a^2 - 18174a^2/T^L] \quad \text{(E4)}$$

where a is loading of the solvent, T^L is the temperature of the liquid phase, and x_{PZ} is molar fraction of the solvent in liquid phase. As aerosols move through the bulk liquid phase, drag force is also important [28]:

$F_D = 0.5\rho^G V_{rel}^2 C_D A_{proj}$, (E5)

where C_D is drag coefficient, A_{proj} is projected surface area, and V_{rel} is relative velocity. Also, the drop will experience buoyancy and gravity forces. To sum up, acceleration of the aerosol drop will be [28]:

$a_{drop} = (18V_{rel}\,\rho^G/C_C\rho^L\,d_{drop}) - [1 - \rho^G/\rho^L]g$ (E6)

where d_{drop} is the diameter of the drops, g is the gravity constant, and C_C is Cunningham slip corrective factor. Sherwood and Nusselt numbers are given as [28]:

$Sh^G = 2 + 0.6\,(Re^G)^{0.5}\,(Sc^G)^{1/3}$, (E7)

$Nu^G = 2 + 0.6\,(Re^G)^{0.5}\,(Pr^G)^{1/3}$, (E8)

where Re is the Reynolds number, Sc is the Schmidt number, and Pr is the Prandtl number.

The resultant heat and mass transfer equations are depicted below (equations E9, E10, and E11, accordingly) [28]:

$$\frac{dn_i}{dt} = \phi\, k_{g,i}\, A_{Drop}\, \frac{\left(P_i^G - P_i^*\right)}{RT^G} = \phi\, 2\,\pi\, d_{Drop}\, D_i^G\, \frac{\left(P_i^G - P_i^*\right)}{RT^G}$$

$$\frac{dn_{CO_2}}{dt} = k_g'\, A_{Drop}\left(P_{CO_2}^G - P_{CO_2}^*\right) = 2\,\pi\left(d_{Drop}\right)^2 k_g'\left(P_{CO_2}^G - P_{CO_2}^*\right)$$

$$n_{Tot}\overline{Cp}_{mix}^{L}\frac{dT^L}{dt} = h^G\, A_{Drop}\left(T^G - T^L\right) + \sum_i^{Nc}\frac{dn_i}{dt}\left(\overline{H}_i^{\,G} - \overline{H}_i^{\,L}\right)$$

In equation E9, Φ is defined as:

$$\Phi = 0.75\,(1 + Kn)/(Kn^2 + Kn + 0.283Kn + 0.75), \quad \text{(E12)}$$

in turn

$$Kn = \lambda / d_{drop}, \quad \text{(E13)}$$

where λ is the mean free path of the molecules. In equations E9, E10, and E11, n_i represents aerosol mole number, k_g is mass transfer coefficient, which can be found using Nusselt number, and h^G is the enthalpy of the gas phase [28].

Two cases were studied: in first, an intercooler was implemented in the middle of the absorber column, in the second case, there was no intercooler. Their schematic representation is illustrated in figure 2.2.

Figure 2.2: Schematic representation of two absorbers simulated in Aspen Plus. Retrieved from Fulk and Rochelle [28] .

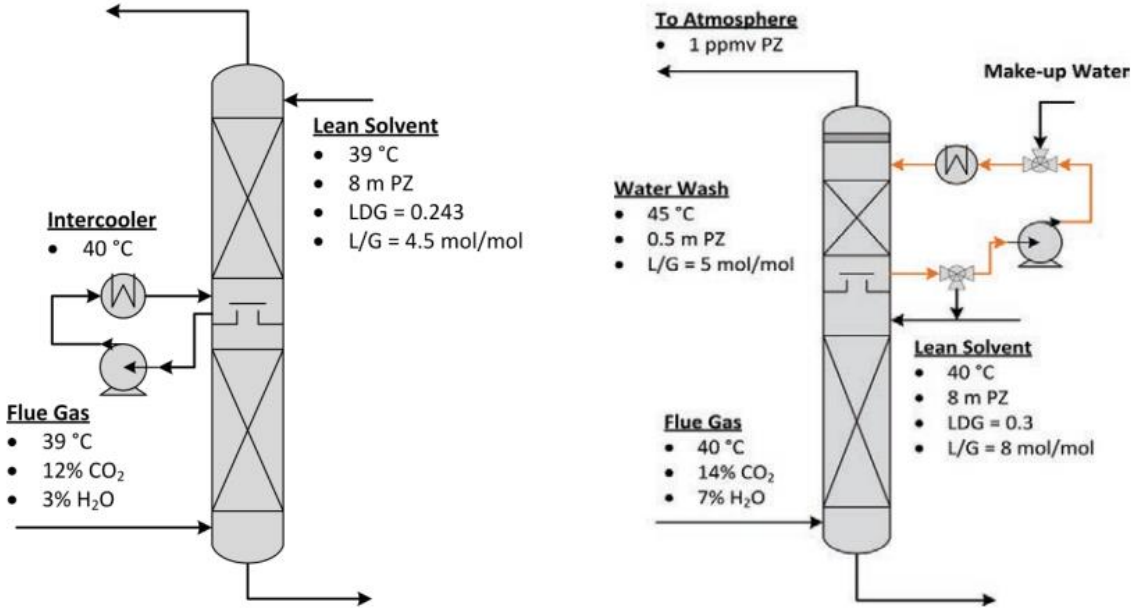

As a result, the authors provided pressure, temperature, and diameter profiles. Figure 2.3 demonstrates aerosol size over height of the column (Z/Z_{tot} represents

height fraction). As it can be seen in figure 2.3, droplets become larger to the top of the column, which is reasonable, as due to temperature decrease saturation increases. Also in case of presence of the intercooler, formation of aerosols was suppressed. According to the authors, this happened because intercooler provided condensation of gaseous PZ. Concluding, this study is a valuable contribution as it deduces important mass and heat transfer equations and provides with suitable assumptions.

Another endeavor to model aerosol based emissions using a process simulator was made by Khakharia and his colleagues [58]. They also used Aspen Plus commercial software to simulate aerosol formation in a typical CO_2 capture column using MEA as a solvent. The authors assumed that liquid flows downwards through the column, and gas phase and aerosols flow upwards. As Aspen Plus do not allow synchronous calculations among three phases (liquid, gas, and aerosol), it was presumed that the aerosol droplets do not interfere with the liquid coming from the top of the column. The constructed flowsheet part is illustrated in figure 2.4. Gas-liquid interaction was modelled in a rate-based absorption column, whereas aerosol-gas interaction was modelled in a PFR. Then aerosol-gas phase was separated in a flash drum to be delivered to the second absorption column. This operation was repeatedly carried out for every column stage.

Figure 2.3: Diameter of the aerosol drops against height of the column. IC curve represents the case with the intercooler, NIC – without the intercooler. Retrieved from Fulk and Rochelle [28].

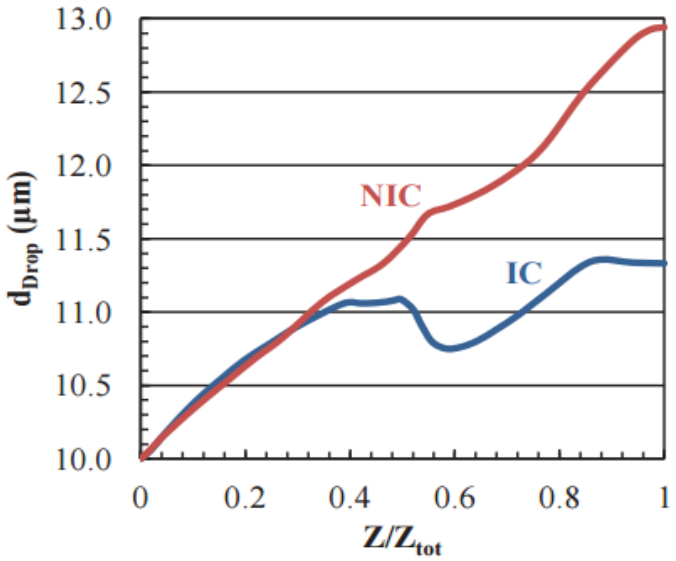

Figure 2.4: Aspen Plus flowsheet to model aerosol-based amine emissions. Retrieved from Khakharia et al. [58]

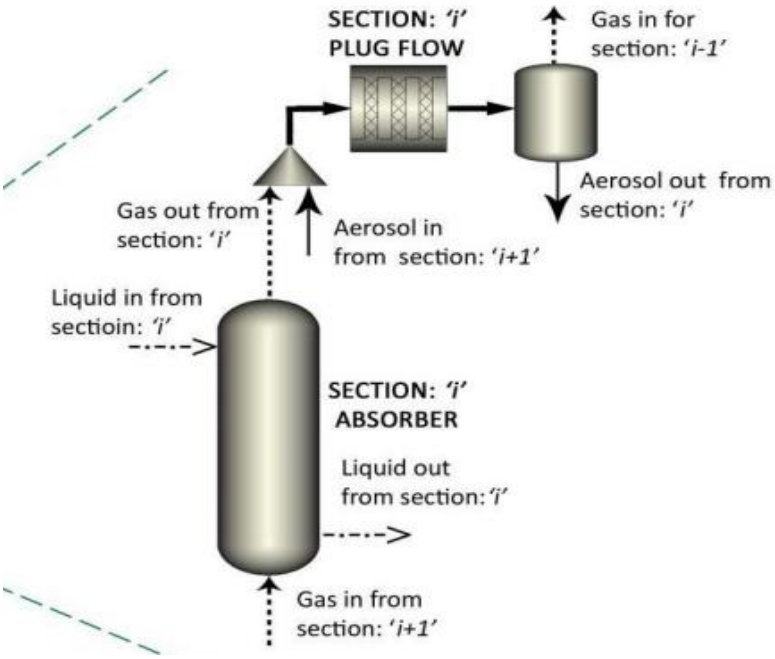

Specifications of the feed gas and MEA are demonstrated in table 2.1. Thermodynamic model was chosen to be NRTL [58]. Reactions taking place are depicted in table 2.2.

The results confirmed that at the top of the column, value of S increases which is a favorable condition for formation of aerosols. Feed gas concentration of carbon dioxide was varied to observe its effect on the emissions. Increasing concentration of CO_2 led to decreased emissions. Also increase in solvent temperature caused decrease in aerosol emissions [58]. If Fulk and Rochelle [28] concentrated on theoretical part, Khakaria and co-authors [58] provide extensive methodology to carry out the process simulations.

Table 2.1: Specifications of flue inlet gas to the absorption column. Retrieved from Khakharia et al. [58]

Parameter	Flue gas	Solvent
Temperature (°C)	48	40
Flow rate (kg/sec)	616	2341
Pressure (bar)	1.016	1.016
Loading (mol CO_2 / mol MEA)	-	0.23
	Composition	
Molecule	mole fraction (Flue gas)	mass fraction (Solvent)
H_2O	0.1127	0.655
MEA	-	0.295
CO_2	0.133	0.05
N_2	0.7162	-
O_2	0.0381	-

Table 2.2: Reactions that occur during CO_2 capture. Retrieved from Khakharia et al. [58]

Reaction name	Stoichiometry
	Equilibrium
Water Dissociation	$2\ H_2O \leftrightarrow\ H_3O^+ + OH^-$
CO_2 hydrolysis	$CO_2 + 2\ H_2O \leftrightarrow\ H_3O^+ + HCO_3^-$
Bicarbonate dissociation	$HCO_3^- + H_2O \leftrightarrow H_3O^+ + CO_3^{2-}$
Carbamate Hydrolysis	$MEACOO^- + H_2O \leftrightarrow MEA + HCO_3^-$
Amine Protonation	$MEA^+ + H_2O \leftrightarrow\ \ MEA + H_3O^+$
	Kinetic
Carbamate formation	$MEA + CO_2 + H_2O \rightarrow MEACOO^- + H_3O^+$
Bicarbonate formation	$CO_2 + OH^- \rightarrow HCO_3^-$

Although last two studies were conducted independently, they complement each other in a way that enables the successors to carry out calculations and Aspen Plus simulations of aerosol formation.

As it was stated above, commercial software such as Aspen Plus and MATLAB possess shortcomings to comprehensively model PM which emerge due to supersaturation and form a separate phase. MD simulations can bridge the gap. They can provide understanding of nucleation rate, cluster size, its structure and driving forces behind molecules' behavior. Therefore, this study aims to fill the gap. If previous studies were principally focused on liquid phase, this research concentrates on gaseous phase to simulate PM formation.

Chapter 3 - Materials and Methods

3.1 DESIGN OF THE SIMULATION SYSTEM

With the aim of methodological study of formation of aerosols, several systems with different configurations of components in vapor phase were considered. In a typical PCCC column, which is at 60^{o}C and 1 bar, the components present in the gaseous phase and their concentrations were determined experimentally by Khakharia [59] and are mentioned in table 3.1.

Table 3.1: The components present and their concentrations in a typical PCCC in the gas phase at 60 ^{o}C and 1 bar [59].

Components	Molar fractions
MEA	3.7×10^{-5}
CO_2	0.04
H_2O	0.18
N_2	0.73
O_2	0.04
SO_2	0.000047
Ar	0.000054
H_2SO_4	1.5×10^{-13}

Initially, molecular simulations were conducted using gaseous CO_2 and liquid MEA to test and verify selected forcefield parameters. Further, the mixtures of

MEA and CO_2 were simulated at the compositions mentioned in table 3.2 (system I). The formation of MEA/CO_2 PM is feasible under supersaturation condition, which occurs when concentration of non-condensable component is much higher than the concentration of condensable constituent. To facilitate such condition, number of MEA (condensable component) molecules were increased while CO_2 concentration is maintained the same (systems II and III in table 3.2). It should be noted that since MEA in liquid phase was neglected in following simulations, the study does not focus on CO_2 absorption. Moreover, the simulations were performed with the presence of water, nitrogen, oxygen, and sulfur dioxide (system IV and V), sequentially to rigorously imitate the condition in the absorption column and to investigate the effect of individual components on the dynamics of PM formation. Argon and sulfuric acid were not used in the simulations because of their inert nature and extremely low concentrations, respectively. In systems IV and V, the concentrations of the components complied with experimental values in table 3.2, except for SO_2. The number of molecules SO_2 was set to 10 (although it is ten times higher than its concentration in reference to table 3.2) in system V to be able to completely capture the effect of the components within reasonable simulation time frame.

Table 3.2: The number of molecules of individual components chosen to simulate different systems to systematically explore the aerosol formation in typical PCCC.

Systems	Number of molecules					
	MEA	CO_2	H_2O	N_2	O_2	SO_2
A	1000	-	-	-	-	-
B	-	1081	-	-	-	-
I	1	1081	-	-	-	-
II	10	1081	-	-	-	-
III	25	1081	-	-	-	-
IV	1	1081	4865	19730	1081	-
V	1	1081	4865	19730	1081	10

3.2 TEST FOR SUPERSATURATION

Before performing molecular simulations, a separate process simulation was carried out to calculate supersaturation, the critical concept described in chapter 1. For this purpose, versatile and popular process simulator Aspen Plus was utilized. The method to identify supersaturation for the mixtures was based on the work presented by Imle et al. [60]. Conventional CO_2 absorption by MEA process flowsheet using ELECNRTL thermodynamic model was a starting point for the simulations.

The process flowsheet is depicted in the figure below.

Figure 3.1: Aspen Plus flowsheet to calculate saturation ratio for the systems.

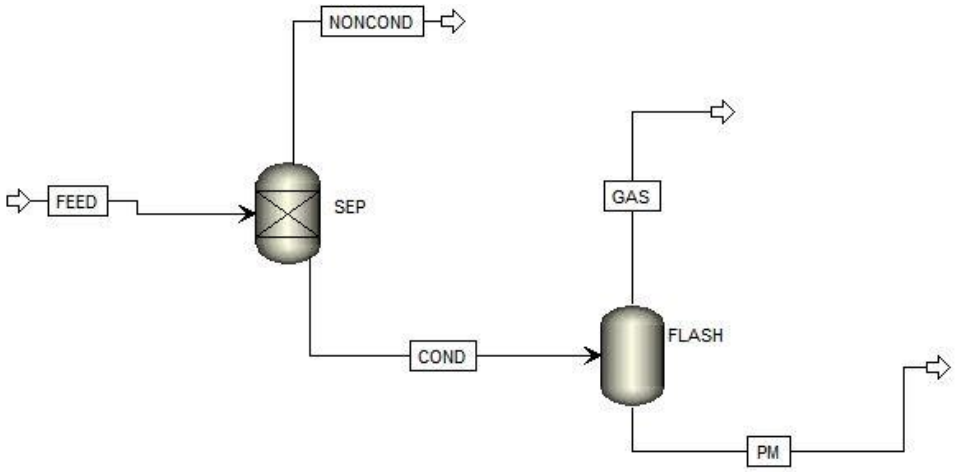

The flow rate of the feed was adjusted according to molar fractions of the components. For example, the feedstock in case of system I was 1 kmol/hr of MEA and 1081 kmol/hr of CO_2. Similar proportions were maintained for the other systems. The feed at atmospheric pressure was directed to a separator block, which is named as SEP in figure 3.1. It separated condensable and non-condensable components of the feed. A condensable component is defined as a gaseous substance which readily forms liquid droplets under compression [60]. Within the framework of this research condensable components under consideration include water and MEA. Then, these components were fed into an isothermal adiabatic flash, which operates at 333 K. Vapor fraction was set 0.9999. The flash establishes vapor-liquid equilibrium and identifies dew pressure of the mixture, which was then used in the equation (E1) to determine saturation values. The results of the simulations are presented in the table below:

Table 3.3: Results of phase equilibrium pressures and saturation values.

System	Molar fraction of MEA	Molar fraction of H_2O	P_{dew} (atm)	S
I	$9.2421*10^{-4}$	0	0.006642	0.139
II	$9.1659*10^{-3}$	0	0.006642	1.379
III	0.0226	0	0.006642	3.402
IV	$3.7372*10^{-5}$	0.1818	0.194187	0.936
V	$3.7359*10^{-5}$	0.1817	0.194187	0.936

3.3 SIMULATION METHODOLOGY

All atom molecular dynamics simulations were performed using GROMACS 5.0.6 package. Simulations were started by placing the appropriate number of gas molecules as reported in table 3.2 in a $10 \times 10 \times 10$ nm^3 box. The box with a low density was specifically chosen to allow faster and better equilibrium conditions. Periodic conditions were applied. Nevertheless, because of low box size, this study cannot quantify solvent losses through PM formation. Energy minimization was conducted using the steepest descent algorithm to begin simulation with a reasonable configuration of molecules. A constraint of the maximum force between molecules of 1000 kJ/mol/nm was used for the energy minimization. Then, system equilibration was carried out with NVT to adjust temperature. The equilibration was performed at 333 K for 100

picoseconds (ps) and the temperature was kept constant with modified Berendsen method. The equilibration was further followed with a long 10 ns production run. Leap-frog integration scheme with a time step of 2 fs was used for all simulations and information about coordinates, velocity and energy were saved every 1.0 ps. For bond parameters, LINCS constraints algorithm with 4^{th} order is used, short range interactions were obtained using electrostatics and van der Waals with a cutoff of 1.5 nm. This value was chosen because of low density of systems under study and based on previous similar studies [61-63]. Particle mesh Ewald method with cubic interpolation and 0.16 nm grid spacing was used to describe long-range electrostatic interactions.

Optimized geometry of all the molecules and their interaction parameters were taken from Automated Topology Builder (ATB) 2.1 server, which derives these parameters from QM calculations and knowledge-based approach. All the parameters were compatible with the standard gromos54a7 forcefield set. Water molecules were modelled with TIP4P model. This model is faster and more robust compared to other popular water models such as SPC and TIP3P [64]. It also yields the most accurate results for water parameters compared to SPC, TIP3P, BF, and ST2 water models [65]. Moreover, several studies in literature confirmed validity of the model to study nucleation processes [66-69]. Interaction parameters for CO_2 and MEA were taken from other references, for reasons that will be presented below. The pair potentials between atoms were

obtained using LJ and Coulomb potential. A simple harmonic potential model was used to compute energies for bonds and angles.

3.4 VALIDATION OF FORCEFIELD PARAMETERS

The accuracy of the force field parameters is an essential part of the proceeding simulations since it affects the properties and interaction between the components. While the parameters generated from the ATB server have been popularly used, several concerns have been raised on partial charges and parameters generated from automated topology generators [70]. In order to validate the parameters of CO_2 and MEA, which are the principal components, simulations of pure CO_2 and pure MEA at 1 bar and 333 K were carried out using the interaction parameters and partial charges as obtained from the ATB server (table 3.4). However, simulations using these parameters resulted in an equilibrium density of the concerned components that substantially differed from the experimental values. The density of MEA and CO_2 as observed from the simulations were 1313.4 kg/m^3 (cf. experimental value of 1024 kg/cm^3) and 24.4 kg/m^3 (cf. experimental value of 1.549 kg/cm^3), respectively. Hence, different sets of parameters were taken from literature for these molecules. The partial charges and other interaction parameters for CO_2 were taken from Cygan et al. [71] and Moosavi et al. [13] and are reported in table 3.4. Similarly, the parameters for MEA were taken as reported by da Silva et al. [52] and Moosavi et al. [13], and are shown in tables A1 and A2 in the appendix. Simulations on

pure components were performed using these parameters and the equilibrium density and self-diffusion coefficients were determined at 333 K and 1 bar and are demonstrated in table 3.5. Diffusion coefficient was determined by fitting Einstein's correlation to the mean squared displacement of the molecules.

Table 3.4: Partial charges and other interaction parameters for CO_2 as obtained from ATB server, Cygan et al. [71] and Moosavi et al. [13]

Parameters	ATB	Cygan et al.	Moosavi et al.
q_C	+0.748	+0.6512	+1.208148
q_O	-0.374	-0.3256	-0.604074
ε_C	0.5698 kJ/mol	0.2340 kJ/mol	0.46708 kJ/mol
ε_O	1.0514 kJ/mol	0.6683 kJ/mol	1.162979 kJ/mol
σ_C	3.0256 Å	2.800 Å	3.358 Å
σ_O	2.7654 Å	3.028 Å	2.8634 Å
k_{CO}	6512 kJ/mol Å^2	8433 kJ/mol Å^2	9718.09 kJ/mol Å^2
r_{oCO}	1.170 Å	1.162 Å	1.162 Å
k_{OCO}	500 kJ/mol rad^2	451.9 kJ/mol rad^2	955.63 kJ/mol rad^2
θ_{oOCO}	180^o	180^o	180^o

The data in table 3.5 reveal that values close to theoretical densities of MEA and CO_2 (1024 kg/m^3 and 1.549 kg/m^3) were observed when the parameters by Moosavi et al. were used. Furthermore, theoretical self-diffusion coefficient for CO_2 is 0.129 cm^2 s^{-1} (at 318K) [72], and theoretical result for MEA diffusion in

water is 1.9655×10^{-5} cm^2 s^{-1} (at 318K) [30]. Obtained values were also in reasonable agreement with the literature data. Hence, in all the succeeding simulations (System I to V) forcefield parameters reported by Moosavi et al. were used.

Table 3.5: Average density and self-diffusion coefficient values for MEA and CO_2 as obtained from three different sets of force field parameters

Component	Source	Density (kg/m^3)	Self-diffusion coefficient ($\times10^{-5}$ cm^2/s)
MEA	ATB	1313.38 ± 11.39	0.003 ± 0.003
	da Silva et al.	1311.90 ±12.54	0.004 ± 0.006
	Moosavi et al.	1094.50 ± 36.27	0.261 ± 0.005
CO_2	ATB	24.41± 0.10	370.32 ± 43.19
	Cygan et al.	1.45 ± 0.10	1556.85 ± 1171.86
	Moosavi et al.	1.624 ± 0.10	15550.96 ± 436.89

Chapter 4 - Results and Discussion

In all systems except system I formation of clusters was observed during the simulation. In essence, these molecular clusters start to nucleate in gas phase and eventually form particles to emerge as a separate phase. Initially, several clusters of molecules were found, however, by the end of the simulation (10 ns), all these clusters merged to form large particles containing all MEA molecules, more than 90% of CO_2, majority of water molecules, and SO_2 present in the system. The analysis will begin by pictographically presenting the time evolution of molecular clusters in different systems. Then quantitative examination of the clusters will be performed. Lastly, structural analysis of the formed particles will be carried out using interaction potential between molecules and the radial distribution function.

4.1 VISUAL ANALYSIS

Figure 4.1 shows snapshot of system I (a) after energy minimization (b) at the end of NVT equilibration (0.1 ns) (c) an intermediate step (0.1 ns) of the MD simulation and finally (d) at the end of 10 ns simulation run. As observed all molecules were initially placed randomly and after 0.1 ns of NVT simulation the molecules are still distributed randomly (figure 4.1 b). Finally, the MD run which was carried for 10 ns, also does not show any formation of clusters as seen in figure 1 c and d (at 0.1 ns of 10 ns, respectively).

Figure 4.1: Snapshots from the simulation with 1 MEA and 1081 CO_2, system I, at 333K: (a) after energy minimization (b) at the end of NVT equilibration (0.1 ns) (c) an intermediate step (0.1 ns) of the MD simulation and finally (d) at the end of 10 ns simulation run. CO_2 molecules are shown with lines and MEA molecule by the vdW spheres of each atom.

Representation:  Monoethanolamine (MEA)  CO_2

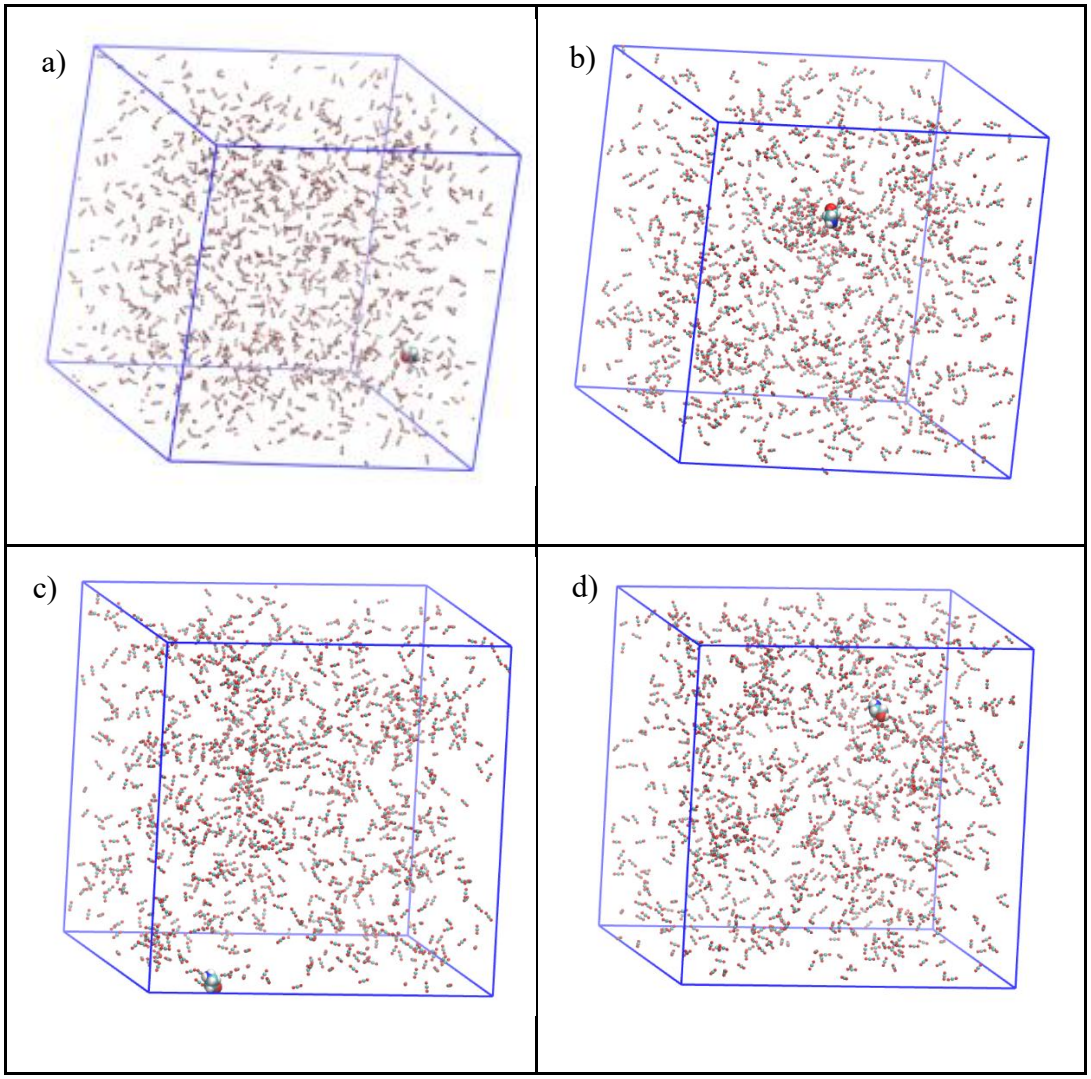

Figure 4.2: Snapshot from the simulation with 10 MEA and 1081 CO_2, system II, at 333 K: (a) after energy minimization (b) at the end of NVT equilibration (0.1 ns) (c) an intermediate step (0.1 ns) of the MD simulation and finally (d) at the end of 10 ns simulation run.

Representation: CO_2 Monoethanolamine (MEA)

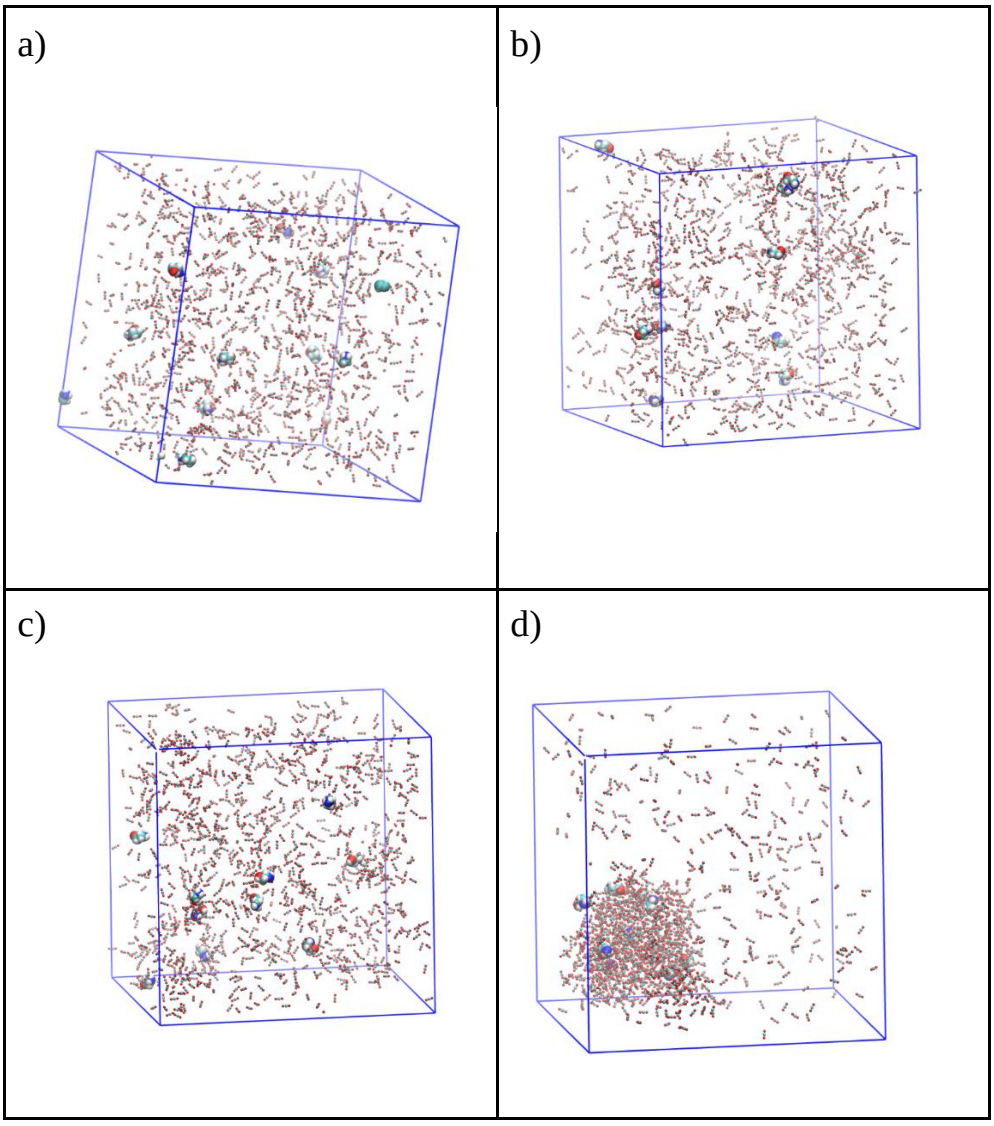

However, interestingly, at a higher MEA concentration, formation of distinct clusters was observed as shown in figure 4.2 for system II and in figure 4.3 for system III. These particulates essentially contain all MEA molecules and majority of CO_2 molecules. Apparently, the formation of the particle cluster can

be correlated with the higher degree of supersaturation in systems II and III, as compared to system I. These values were calculated in chapter 3.2 and are: 1.379, and 3.402 against 0.139, respectively. These observations on cluster formation make sense as saturation value for single condensing component above 1 is required for particle nucleation that starts with cluster formation.

Figure 4.3: Snapshot from the simulation with 25 MEA and 1081 CO_2, system III, at 333K: (a) after energy minimization (b) at the end of NVT equilibration (0.1 ns) (c) an intermediate step (0.1 ns) of the MD simulation and finally (d) at the end of 10 ns simulation run.

Representation: CO_2 Monoethanolamine (MEA)

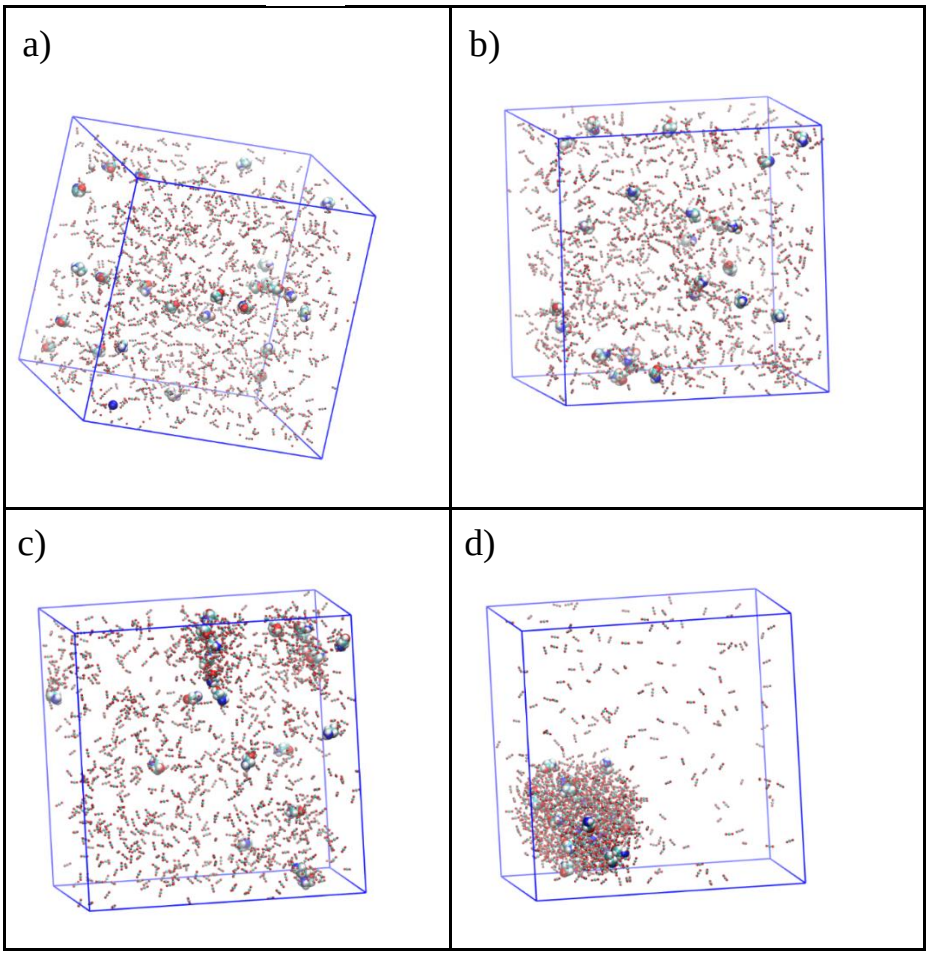

Noticeably, final particulate cluster formed in system III is larger compared to the cluster of system II. Approximate diameters of the aerosol particles after 10 ns are 3.8 nm and 4.6 nm for system II and III, respectively.

Visual analysis using VMD revealed that for system IV (see figure 4.4) presence of air do not significantly affect the cluster formation rate. In the 10 ns run two clusters were formed: one large and one small. These formed PM are made of CO_2, H_2O, and MEA molecules. Herein, it should be noted that, although they are not shown in the figure for clarity, all nitrogen and oxygen molecules were not attached by any of the cluster forming molecules (MEA, CO_2, or water), which shows nitrogen and oxygen were not involved in nucleation processes.

Figure 4.4: Snapshot from the simulation with 1 MEA, 1081 CO_2, water, nitrogen, and oxygen molecules, system IV, at 333K: a) NVT ensemble at initial frame, b) NVT last frame, c) MD at 100th frame d) MD at 5000th frame

Representation: CO_2 Monoethanolamine (MEA) Water

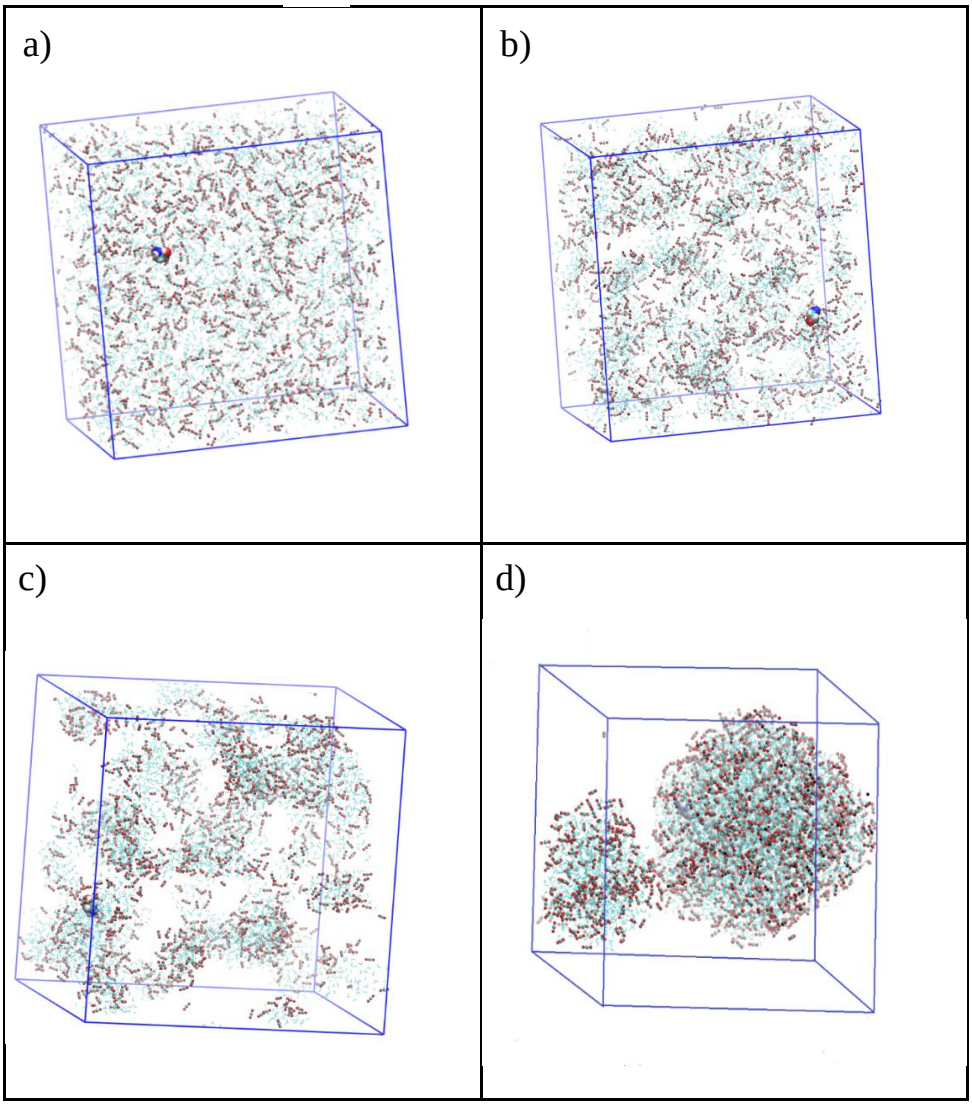

Figure 4.5: Snapshots from the simulation of system V containing MEA, CO_2, water, nitrogen, oxygen, and sulfur dioxide molecules at 333K: (a) after energy minimization (b) at the end of NVT equilibration (0.1 ns) (c) an intermediate step (0.1 ns) of the MD simulation and finally (d) at the end of 10 ns simulation run.

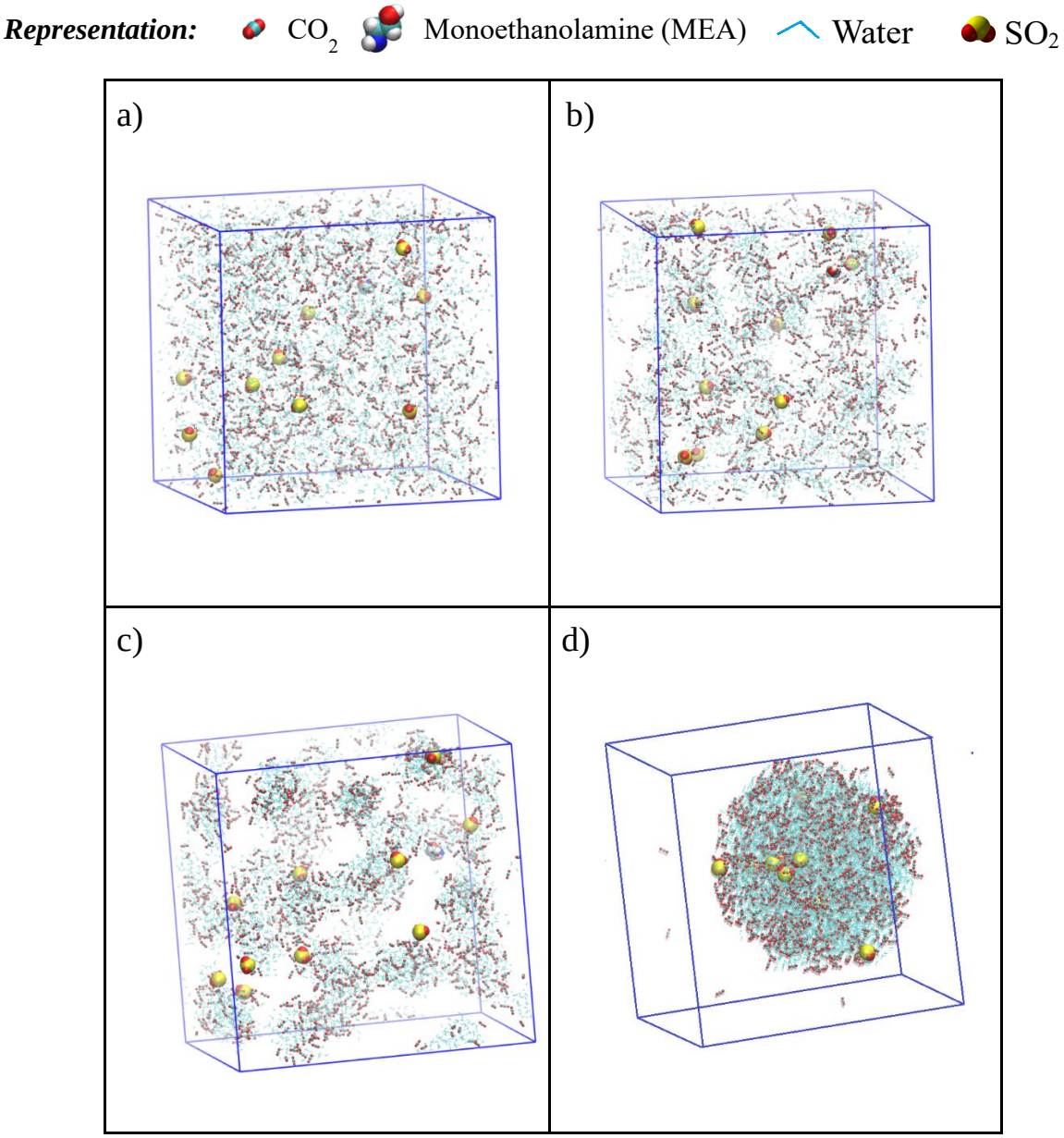

Figure 4.5 shows snapshots of simulation of system V, which contains 10 SO_2 molecules in addition to the molecules of system IV. It can be seen that SO_2 molecules did not noticeably influence cluster formation rate, and that all the

sulfur dioxide molecules were finally captured in the formed cluster. Comparing figures 4.4 and 4.5 to the figures 4.1, 4.2 and 4.3, it is evident that even in presence of air and other components, most of the CO_2 molecules are absorbed in the MEA clusters formed. For both systems IV and V, clusters were formed even if the system was sub saturated according to equation E2.

4.2 QUANTITATIVE ANALYSIS OF THE CLUSTERS

A quantitative analysis of the cluster was performed to identify formation rate of the clusters. Specifically, the *clustsize* function in GROMACS package was used to examine size distribution of clusters and cluster growth rate in all the five systems. A separate analysis was done also on the NVT equilibration part of the simulation, as few clusters were observed during this period too. Quantitative assessment of the clusters was carried out in terms of CO_2 molecules. The *clustsize* code counts a single molecule also as a cluster, wherein the criteria for considering clusters was chosen when molecules of CO_2 are at distance of 0.7 nm from each other. As the molecules cluster together, the overall number of clusters decreases. The results of the analysis are shown below:

Figure 4.6: The number of clusters decreases forming larger clusters for all the systems, except system I, with time during the (a) NVT ensemble (b) 10 ns MD simulation run.

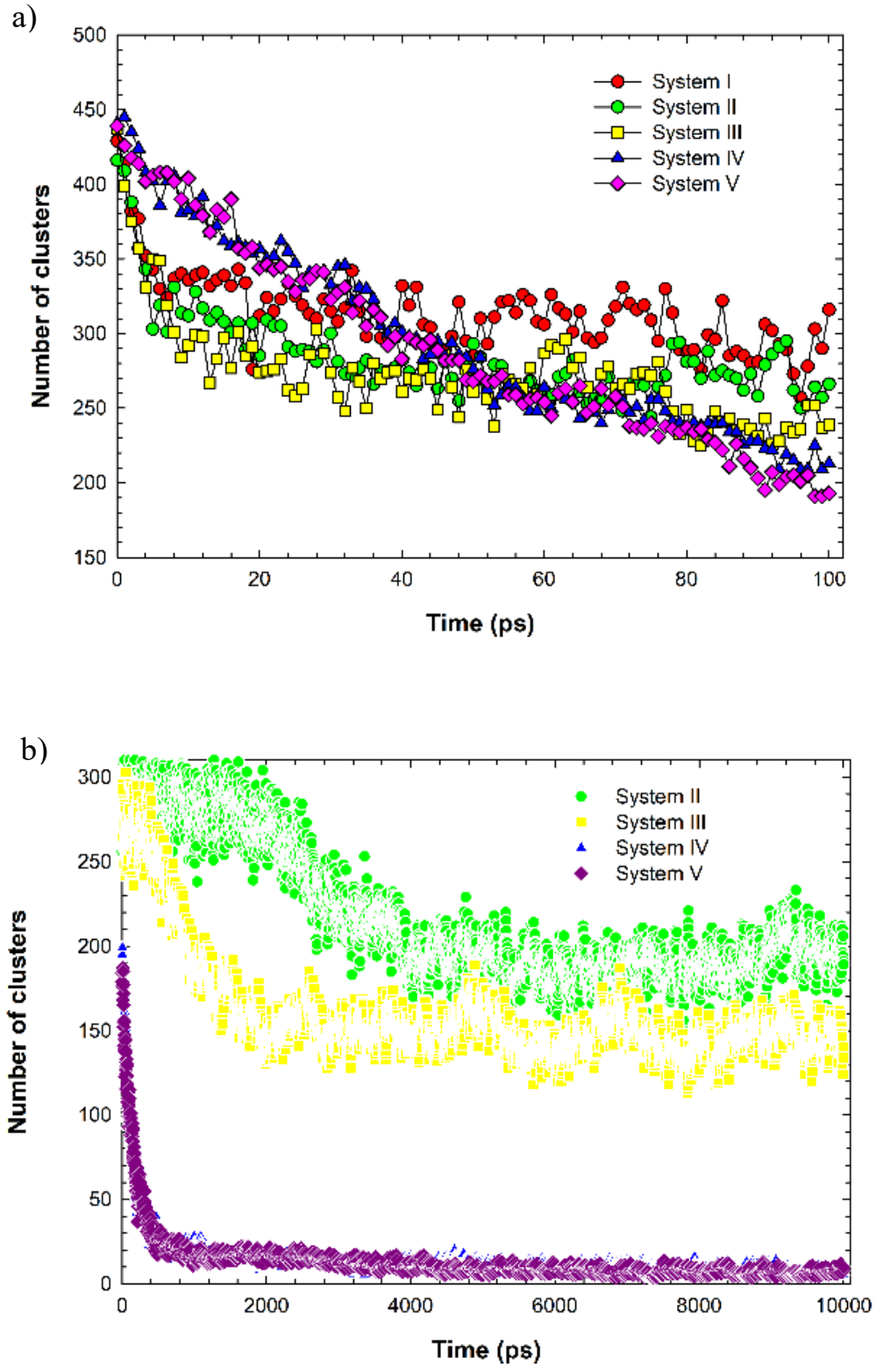

As it can be seen in figure 4.6 a, during the 100 ps of NVT simulation, the number of clusters of molecules decreased significantly for all five systems, which indicates the coalescence of the clusters. Particularly, number of cluster decreased from 450 originally to about 250 for all the systems (except system I, for which it was 350), which means majority of the molecules were attracted to each other at a distance less than the cutoff length. Comparing three systems with only MEA and CO_2, it is noticeable that clustering effect is similar for systems II and III; however, in case of the presence of air components and SO_2 cluster formation rate is fast with a high slope. Similar analysis was performed for the MD simulation, which was for further 10 ns beyond the NVT ensemble. The results for system I is not included herein, as it did not form any cluster and consequently, the number of clusters remained same throughout the simulation. The results shown in figure 4.6 b suggest that a higher concentration of MEA (comparing system II and III) leads to faster cluster formation. Moreover, the presence of air and water accelerates the cluster formation. The graph for systems IV and V overlap, indicating that the presence of SO_2 molecules do not alter the growth dynamics.

Next, the number of CO_2 molecules in the largest cluster is determined, that is in the formed particulate matter. During the NVT part of the simulation, number of CO_2 molecules in the largest cluster changed abruptly through time as can be observed from figure 4.7 a. Due to severe fluctuations a simulation of

longer time is needed to make definite conclusions, which are shown in figure 4.7 b for the longer 10 ns MD run.

Comparing systems II and III (figure 4.7 b), it can be concluded that number of molecules involved in the largest cluster increases with increasing MEA molecules, supporting the previous conclusions from chapter 4.1, that more MEA molecules contribute to the creation of larger clusters. Thus, it can be concluded that the concentration of the MEA in the lean solvent which is typically 30 wt% (or 10 mol%) could be an optimization parameter for controlling the particle formation during PCCC processes. Altering the lean solvent concentration will impact the amount of the water and MEA evaporated to the gas, and therefore the particle nucleation rate will change. Furthermore, the maximum number of CO_2 molecules in system IV is characterized by breaks in the graph, which represent coalescence and dissociations of the largest clusters. On the other hand, addition of SO_2 molecules facilitated formation of stable clusters. It should also be noted that there were two clusters formed in system IV (as observed visibly), therefore maximum number of the molecules in the largest cluster is less than of system V.

Finally, combining figures 4.6 b and 4.7 b, for systems II and III, MD simulations reveal that at 10 ns there are 189 and 134 clusters, while the largest clusters contain 799 and 921 CO_2 (cf. a total of 1081 CO_2 molecules are in the box) molecules, respectively. In other words, for both systems, there is one large cluster, which is surrounded by the remaining 282 and 160 CO_2 molecules some

of which was considered by the program as clusters as they were less than 7 Å apart.

Figure 4.7: Number of molecules in the largest cluster increasing with time during the (a) NVT ensemble (b) 10 ns MD run.

a)

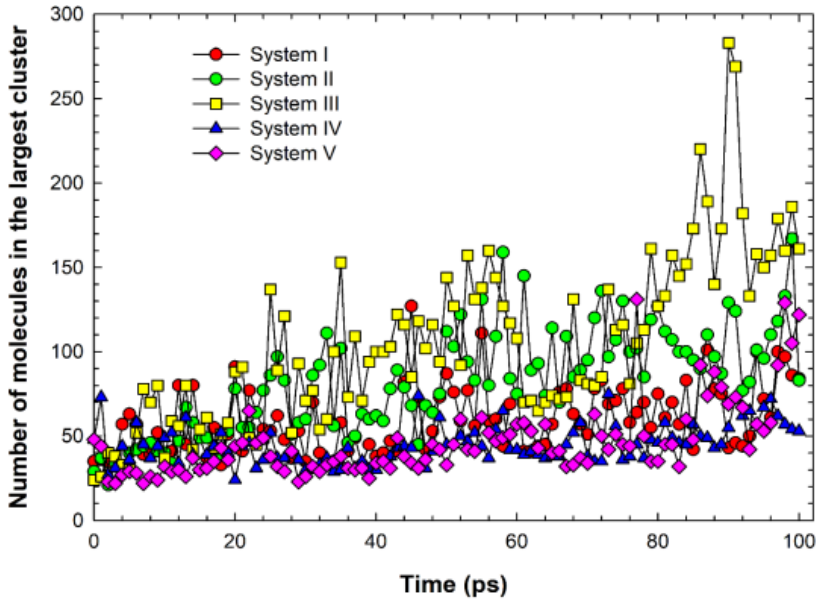

b)

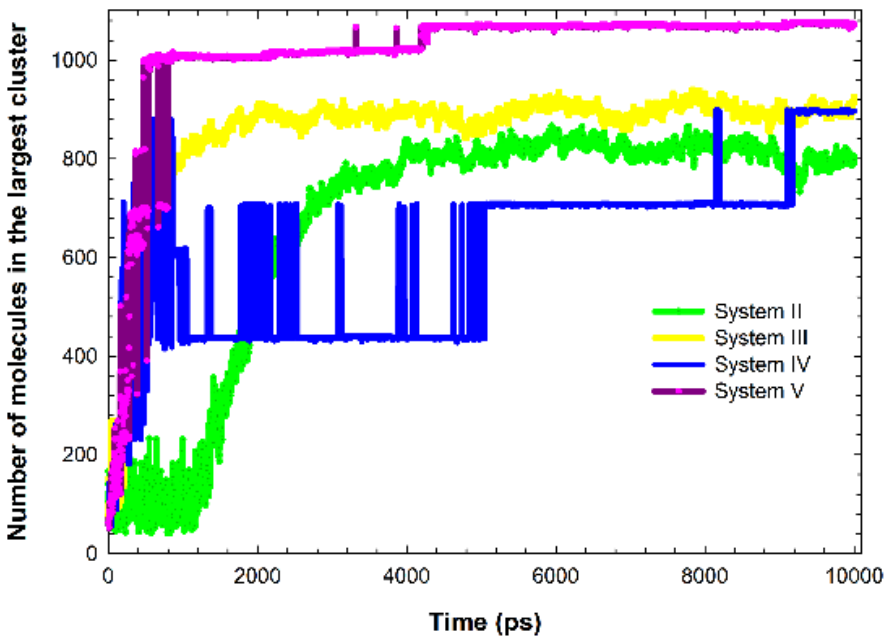

In system IV, the largest cluster includes 897 CO_2 molecules and remaining portion of carbon dioxide are in the smaller cluster. With SO_2 addition final large cluster formed at around 800 ps, which further grew and contained 1072 CO_2 molecules towards the end of 10 ns run.

4.2.1 Nucleation rate

Cluster size analysis can also be used to identify nucleation rate of the PM formed. Herein nucleation rate was defined using a combination of methods suggested by Stauffer et al. [73] and Yasuoka and Matsumoto [74]. Initially, a moment was selected when the PM is formed and stable using VMD and figure 4.7 b. Then the number of molecules inside PM was identified using VMD and *clustsize* function. Finally, MS Excel was used to find the slope of the graph number of clusters versus time. Figure 4.8 below depicts PM growth trend in systems II and III in terms of all molecules constituting it.

Figure 4.8: Number of molecules per unit time for systems II and III.

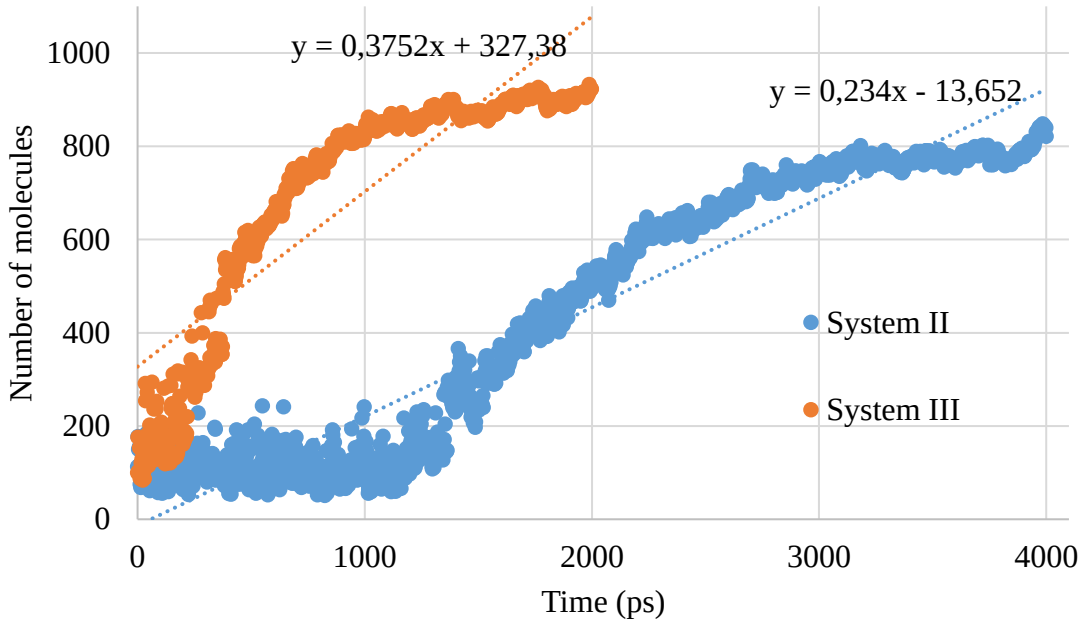

From the figure above, nucleation rates of PM in systems II and III are:

$J_{II} = 0.234 \times 10^{30}$ cm^{-3} s^{-1}

$J_{III} = 0.3752 \times 10^{30}$ cm^{-3} s^{-1}

For system IV, there were two clusters formed, therefore, it is not possible to calculate nucleation rate since GROMACS can identify only the number of molecules in the largest cluster. In case of system V, number of water and SO_2 molecules were determined separately. Then, they were added to give the total number of molecules in the largest cluster (PM).

Figure 4.9: Number of molecules per unit time for system V.

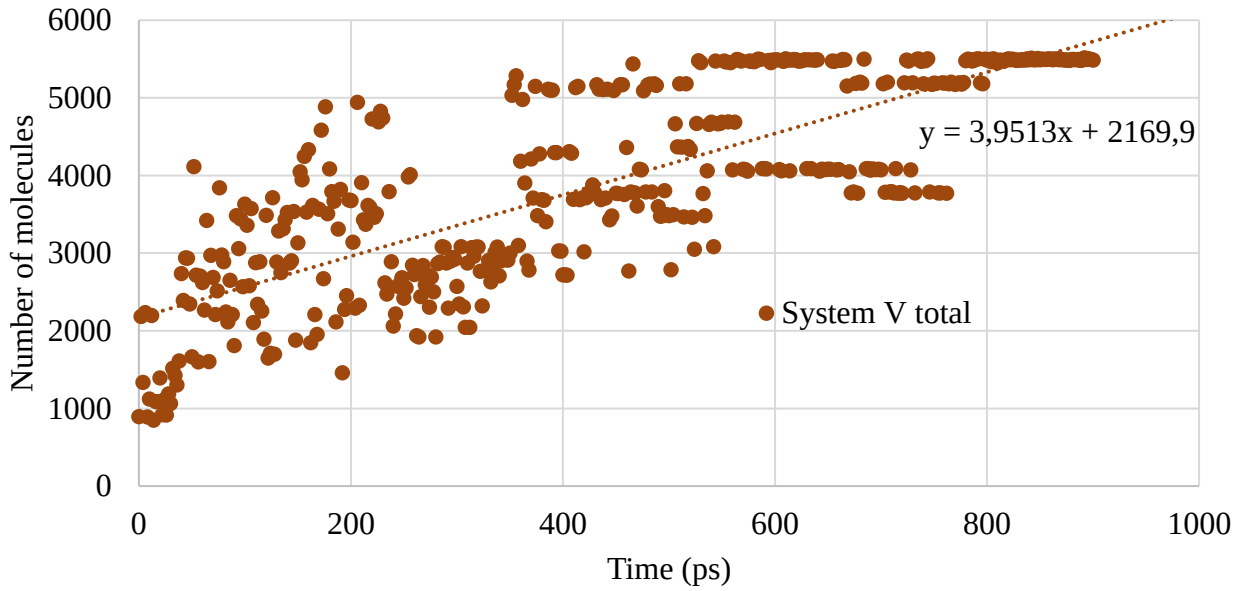

Hence, nucleation rate of PM in system V is:

$J_V = 3.9513 \times 10^{30}$ $cm^{-3}s^{-1}$.

In general, nucleation rates range over several orders of magnitude depending on the method used to determine the rate [75, 76]. For example, for water,

experimental value for nucleation rate was observed to be three orders of magnitude less than the value obtained by classical nucleation theory (CNT) [76]. Yasuoka and Matsumoto [74] studied homogeneous nucleation of water in an argon media using MD simulations and reported seven orders of magnitude difference compared to the theoretical value. In another study, Yasuoka and Matsumoto [77] also used MD simulations implementing NVT ensemble to identify nucleation rate of water at 350 K. They calculated the nucleation rate to be 4.21×10^{29} $cm^{-3}s^{-1}$ compared to the value calculated using CNT which is 3.7×10^{28} $cm^{-3}s^{-1}$. Horsch et al. [78] used Yasuoka and Matsumoto method and reported nucleation rate for CO_2 at 269 K to be 4.1×10^{27} $cm^{-3}s^{-1}$ and compared to its value predicted by CNT (2.5×10^{27} $cm^{-3}s^{-1}$). In general, CNT model for nucleation rate differs from experimental values up to 26 orders of magnitude whereas MD simulation resultant rates vary from experimental values up to 14 orders of magnitude [76]. Considering such substantial deviations, and considering absence of nucleation rate data for CO_2 and MEA under similar conditions, our results are comparable to homogeneous nucleation rate for water at 350 K, and CO_2 at 269 K.

4.3 STRUCTURAL ANALYSIS OF THE CLUSTERS

Radial distribution function (RDF) analysis can shed a light on to the structures of the formed particles. In the following, initially the RDFs between CO_2 molecules for all five systems will be presented and follow it further, with

the detailed energy analysis between the components present in the system. Radial distribution function of C…C pair correlation of CO_2 molecules is demonstrated in figure 4.10. Evidently, all the systems possess a distinct high C…C peak at about 4 Å indicating a packed structure of CO_2 molecules. For system I, as expected, first C…C peak is very weak, and a plain continuation of the RDF refers to uniform distribution of CO_2 molecules inside the box. Comparing systems II and III, first peak is much higher for the latter, which indicates a higher strength of attraction in system III and hence also leads to a larger aerosol particle as noted above. A lower second peak for both systems is observed at 7.35 Å. RDFs of systems IV and V almost coincide, once again supporting the idea that SO_2 has negligible contribution towards aerosol formation. Further comparison of RDFs of system IV and V to systems II and III reveals that presence of water and air components significantly decreases C…C peak, which is reasonable as the components occupy space and hinder $CO_2 – CO_2$ association. Furthermore, the C…C correlation of MEA and CO_2 molecules also demonstrates similar trend as in the previous case (figure 4.11). Nevertheless, all peaks are lower pointing out less interaction between CO_2 and MEA molecules in comparison to $CO_2 – CO_2$ interplay. Apparently, such results are conditioned by high presence of CO_2 molecules and their corresponding hindrance.

Figure 4.10: Radial distribution functions between the carbon atoms of CO_2 molecules for all five systems.

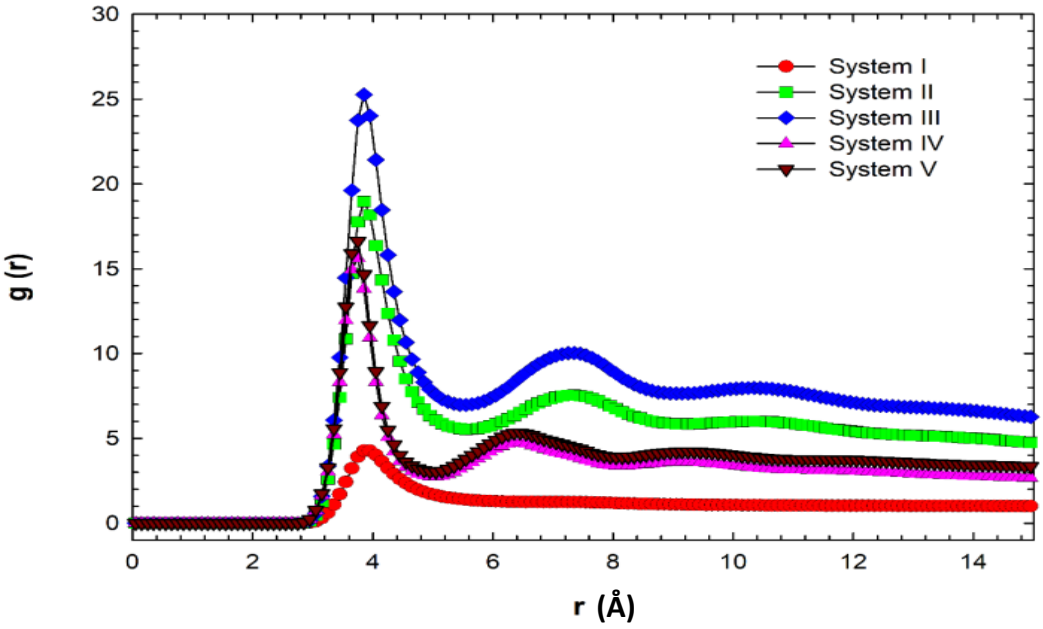

Figure 4.11: RDF between carbon molecules of CO_2 and MEA.

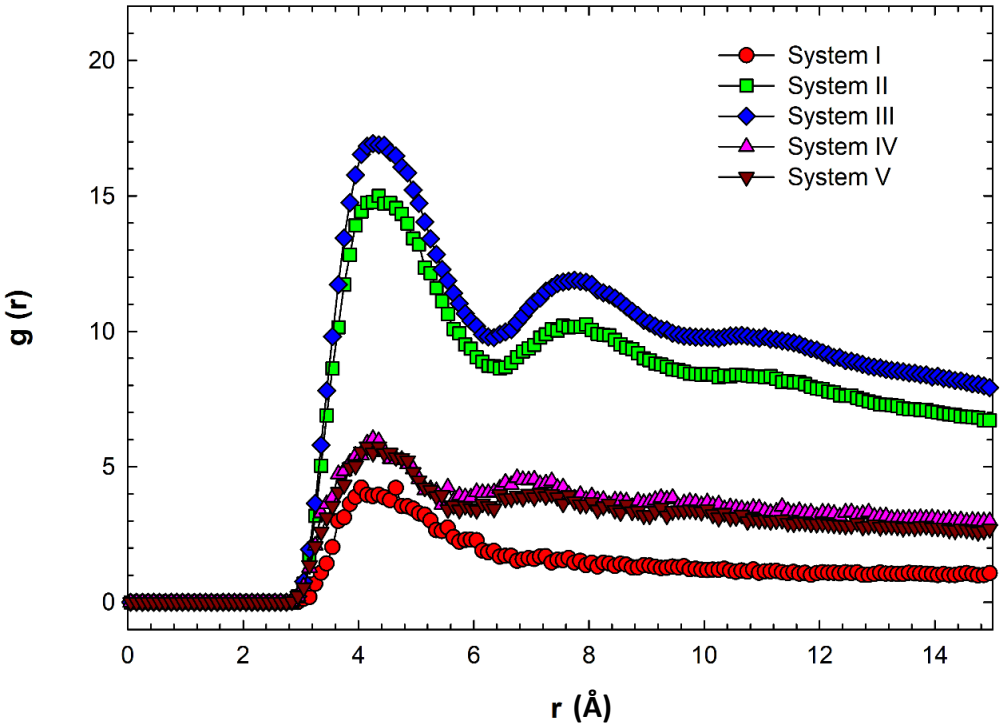

Furthermore, the interaction energies between different components will be explored. A sum of Lennard-Jones and Coulomb interaction energies between all the molecules in the system were evaluated (figure 4.12). Since, MEA – CO_2 and CO_2 – CO_2 interactions are of primary interest, the change in energies among the systems will be assessed and discussed below. Lastly, a discussion will be made on the generalized outcomes of all interaction potentials.

Figure 4.12: Interaction energy between MEA and CO_2 for the five systems. Standard deviation was less than 5% for each system.

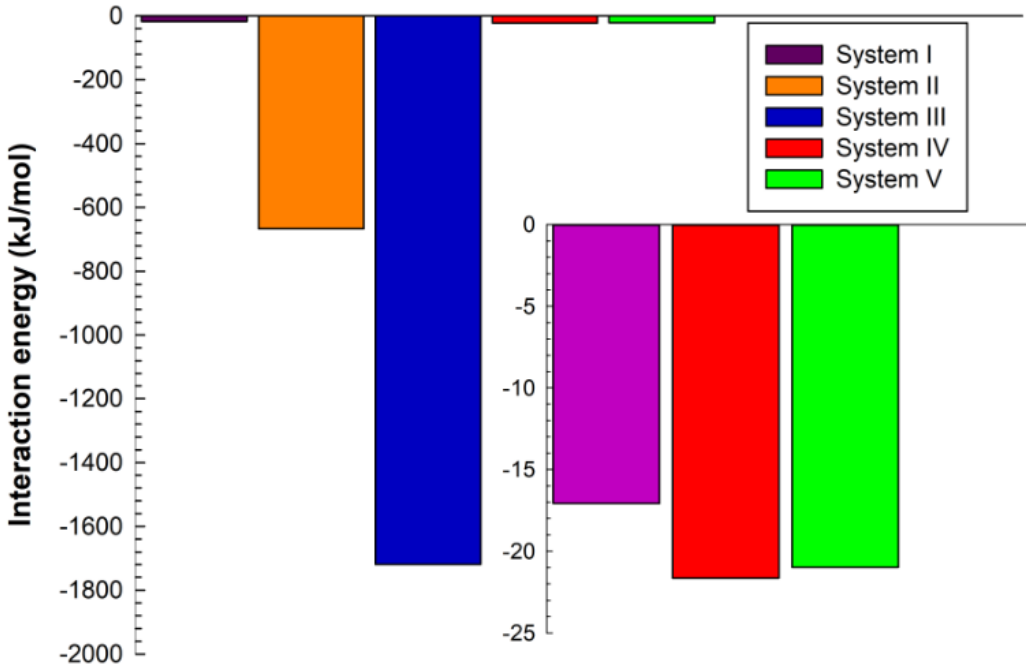

As seen in figure 4.12, there is a strong variation in the MEA – CO_2 interaction energy between different systems and it is highly sensitive to the number of MEA molecules. In first three cases the interaction energy is proportional to the number of MEA molecules: 1, 10, and 25 MEA with -76.7 kJ/mol, -734.3 kJ/mol, and -1874.1 kJ/mol, respectively. Inset in figure 4.12

demonstrates comparison between systems I, IV, and V, each of which has 1 MEA molecule, on a smaller scale to compare. As evident, in the latter two cases MEA – CO_2 has slightly higher energy. Nevertheless, the effect of addition of 10 molecules of SO_2 is negligible.

Figure 4.13: Interaction energy between CO_2 molecules. Standard deviation was less than 5% for each system.

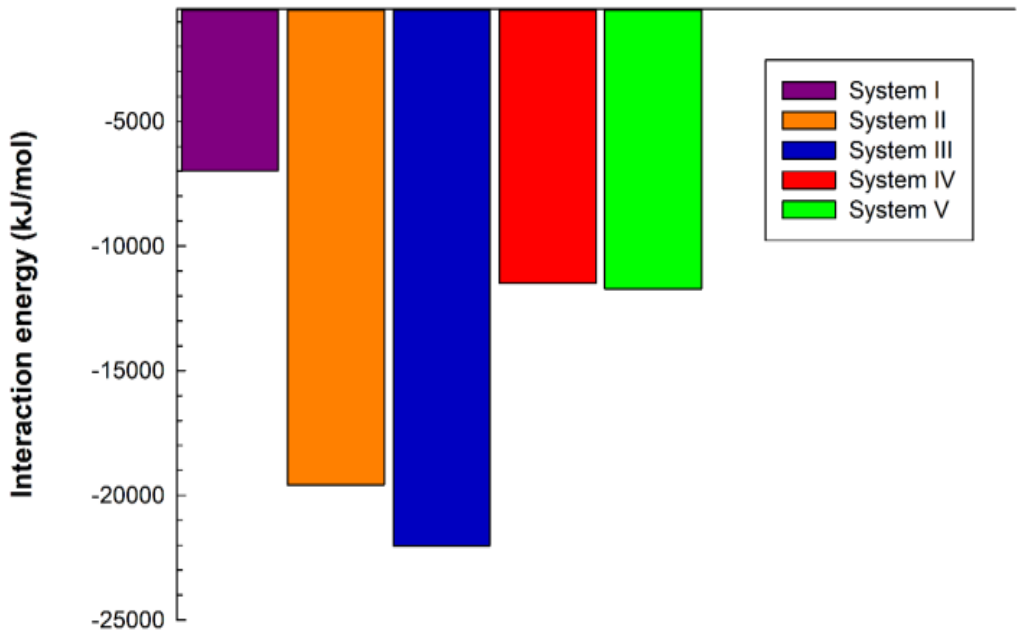

Considering CO_2 – CO_2 interactions, all the systems contain 1081 of CO_2 molecules. The energy of interaction (figure 4.13) in this case is much higher compared to MEA – CO_2. Similar to the results above (figure 4.12), in systems I, II, and III, the potential between CO_2 molecules increases in accordance with MEA number growth. However, the growth rate trend is not proportional. When

air and water are introduced to the systems the CO_2 – CO_2 interactions become weak.

Until now, molecular cluster formation was discussed as governed mainly by MEA and CO_2 molecules. However, energy analysis further reveals that water molecules have considerably high short-range negative Coulomb potential towards both MEA and CO_2 (see table 4.1).

Table 4.1: Energy analysis results for system IV. All units are in kJ/mol.

Components	Coulomb short range	Lennard-Jones short range	Coulomb long range	Lennard-Jones long range
MEA -MEA	-247.92	-0.06	456.95	2.18
MEA - CO_2	-13.27	-8.36	0	0
MEA - N_2	0	-0.55	0	0
MEA - H_2O	**-98.33**	0.66	0	0
MEA - O_2	0	-1.00	0	0
CO_2 - CO_2	-10511.46	-983.22	0	0
CO_2 - N_2	0	-3585.33	0	0
CO_2 - H_2O	**-52010.83**	4463.77	0	0
CO_2 - O_2	0	-821.37	0	0
N_2 - N_2	0	-60683.08	0	0
N_2 - H_2O	0	-2759.39	0	0
N_2 - O_2	0	-14300.64	0	0
H_2O - H_2O	-213907.67	48629.60	0	0
H_2O - O_2	0	-817.50	0	0
O_2 - O_2	0	-1260.29	0	0

Moreover, RDF between water and CO_2 molecules (see figure 4.15) show clear sharp peaks, an articulate sign of strong affinity between these molecules. Also, energy study results mark relatively significant attraction between water and MEA in systems IV and V. For systems IV and V, the number of hydrogen bonds between water, MEA, and CO_2 were calculated and are presented in

figures 4.14, A7, A8, and A9. As can be seen from figure 4.14 below, attraction between water and MEA is also caused by H-bonds formed between them. These findings imply that water plays much more crucial role in shaping the particle formation. On the contrary, considering their large amount, nitrogen and oxygen have no impact in the process. Sulfur dioxide, on the other hand, while being neutral to the others, have a slight affection for CO_2 molecules at short distances, which results from induced dipole-dipole interaction. It is most likely that due to this attraction force SO_2 are inside the formed aerosol particles (PM).

Figure 4.14: Hydrogen bonds between water and MEA in system IV in last 2 ns of MD run. Frames from 4039 to 5039 represent last 2 ns of the MD simulation.

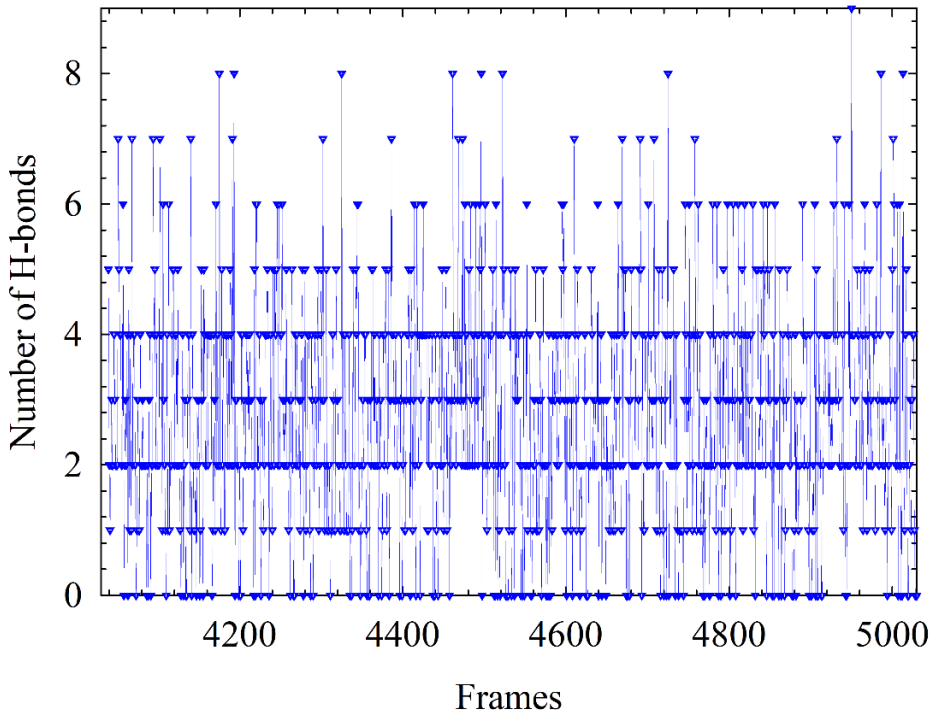

Figure 4.15: RDF between carbon atom of CO_2 and oxygen atom of water.

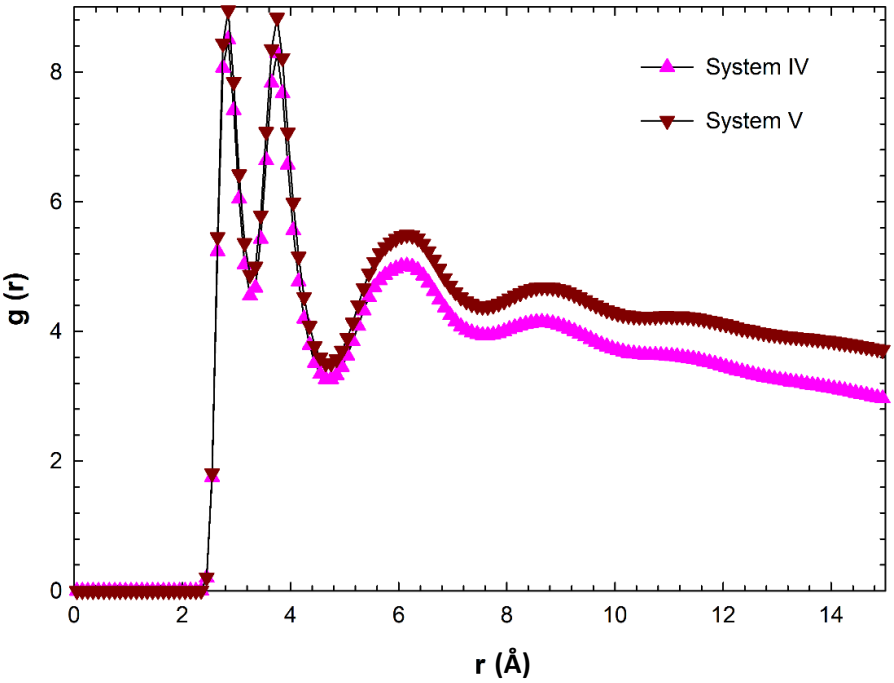

Chapter 5 - Conclusion

This thesis work was carried out for the purpose of understanding of underlying mechanisms and forces that drive particle formation with providing some practical implications to the current issue of amine loss in PCCCs. The simulations demonstrated clear evidence of formation of spherical molecular clusters in four systems out of five, which eventually grows to form larger PM. The formed particles emerge as separate phase and contain all vapor MEA, SO_2, and significant amount of CO_2 and water vapor. In numerical terms formed PM consisted mostly of water and CO_2 molecules, as it was predicted by previous experimental studies. Also, it was found that the presence of water molecules increases formation rate of particulates. Also, higher MEA concentrations in vapor phase promote growth rate and formation of larger clusters (as was suggested in the literature). Energy analysis revealed that CO_2 – CO_2 potential increases with the addition of water and air. As it was already predicted in the literature, CO_2 molecules play critical role in forming PM. Moreover, it was found that nitrogen and oxygen are relatively neutral to the other components. On the contrary, water demonstrates high attractive potential for MEA and CO_2. In addition, RDF analysis of CO_2 and H_2O confirmed packed structure of them inside PM constituting to overwhelming majority of the aerosol particles. Combining RDF and energy analysis results it can be inferred that water vapor probably plays a key role in bringing MEA and CO_2 molecules into the clusters

and keeping them stable. It is also noteworthy that SO_2 molecules were entirely engulfed into the clusters. Furthermore, since customarily CO_2 content in a flue gas is not a process variable, efforts should target vapor MEA and water to reduce particle matter formation in a PCCC column. For example, MEA content in the traditional 30 wt% (10 mol%) aqueous mixture could be altered to an optimum value. Conventional techniques to reduce amine losses in vapor forms could also be effective in tackling the particulate matter formation issue. However, those measures should not lead to increase in saturation of the gas phase.

Furthermore, equation E2 has been repeatedly used in the literature to quantify the saturation ratio of a condensable multicomponent mixture. Nevertheless, as it was stated earlier, the extension of equation E1 to equation E2 may not be fully appropriate for a system with several condensing components as this extension do not have a convincing theoretical basis. In systems IV and V, supersaturation ratio was slightly less than 1, but still there were stable clusters formed which contained all condensable components available. Thus, these findings contradict current supersaturation concept in the literature. In this regard, from theoretical point of view relevance of equation E2 is questionable. Nevertheless, a thorough assessment of equation E2 would require a special comprehensive MD study which should be the purpose of future work.

Also, there are other several suggestions for future studies in this area. Additional MD study should be carried out using NPT ensemble. For additional confirmation, saturation ratio can be directly calculated from MD results. Moreover, considering limitations of this study mainly due to computational restrictions, future research should focus on much larger systems of microscale to be able to evaluate the sizes of PM and quantify solvent losses via aerosol particles in practical terms. Apart from that, increasing time of the simulation can give an idea about lifecycle of PM. Lastly, since MEA/CO_2 relation has been thoroughly understood in this study, various combustion products can be introduced to the systems and their effect on PM can be assessed.

Reference List

1. Baker-Austin, C., et al., *Emerging Vibrio risk at high latitudes in response to ocean warming.* Nature Climate Change, 2012. **3**: p. 73.
2. Gernot, W. and W. Martin L., *Climate Shock: The Economic Consequences of a Hotter Planet*2015, Princeton: Princeton University Press. 243.
3. Zachariadis, T., *Climate Change Impacts*, in *Climate Change in Cyprus: Review of the Impacts and Outline of an Adaptation Strategy* 2016, Springer International Publishing: Cham. p. 25-49.
4. Parmesan, C. and G. Yohe, *A globally coherent fingerprint of climate change impacts across natural systems.* Nature, 2003. **421**: p. 37.
5. Wheeler, T. and J. von Braun, *Climate Change Impacts on Global Food Security.* Science, 2013. **341**(6145): p. 508-513.
6. John, C., et al., *Quantifying the consensus on anthropogenic global warming in the scientific literature.* Environmental Research Letters, 2013. **8**(2): p. 024024.
7. Urry, J., *Climate Change and Society*, in *Why the Social Sciences Matter*, J. Michie and C.L. Cooper, Editors. 2015, Palgrave Macmillan UK: London. p. 45-59.
8. Proceedings of a Joint Symposium by the Board on Atmospheric Sciences and Climate and the Committee on Global Change Comission on Physical Sciences, M., and Resources *Ozone Depletion, Greenhouse Gases, and Climate Change*1988, Washington: National Academy Press. p. 3.
9. *Global Greenhouse Gas Emissions Data*. 2014 [cited 2017 16.11.2017]; Available from: https://www.epa.gov/ghgemissions/global-greenhouse-gas-emissions-data.
10. *Carbon Dioixde*. 2017 14.11.2017 16.11.2017]; Available from: http://climate.nasa.gov/vital-signs/carbon-dioxide/.
11. Sayre, R., *Microalgae: The Potential for Carbon Capture.* BioScience, 2010. **60**(9): p. 722-727.
12. Agency, I.E. *Fossil fuel energy consumption (% of total)*. 2015 16.11.2017].
13. Moosavi, F., F. Abdollahi, and M. Razmkhah, *Carbon dioxide in monoethanolamine: Interaction and its effect on structural and dynamic properties by molecular dynamics simulation.* International Journal of Greenhouse Gas Control, 2015. **37**: p. 158-169.
14. Pires, J.C.M., et al., *Recent developments on carbon capture and storage: An overview.* Chemical Engineering Research and Design, 2011. **89**(9): p. 1446-1460.
15. Agency, U.S.E.P. *Carbon Dioxide Capture and Sequestration: Overview*. 2017 17.11.2017].
16. Herzog, H., *An Introduction to CO2 Separation and Capture Technologies*, 1999, MIT: MIT. p. 1-8.
17. MIT. *Carbon Capture and Sequestration Technologies*. 2016 [cited: 03.12.2016].
18. Markusson, N., S. Shackley, and B. Evar, *The Social Dynamics of Carbon Capture and Storage*, 2012, Routledge: New York.
19. Leung, D.Y.C., G. Caramanna, and M.M. Maroto-Valer, *An overview of current status of carbon dioxide capture and storage technologies.* Renewable and Sustainable Energy Reviews, 2014. **39**: p. 426-443.
20. Vaidya, P.D. and E.Y. Kenig, *CO2-Alkanolamine Reaction Kinetics: A Review of Recent Studies.* Chemical Engineering & Technology, 2007. **30**(11): p. 1467-1474.
21. Alejandre, J., et al., *Force Field of Monoethanolamine.* The Journal of Physical Chemistry B, 2000. **104**(6): p. 1332-1337.
22. S. Hwang, G., et al., *Reaction mechanisms of aqueous monoethanolamine with carbon dioxide: A combined quantum chemical and molecular dynamics study*. Vol. 17. 2014.

23. Han, B., et al., *On the CO2 Capture in Water-Free Monoethanolamine Solution: An ab Initio Molecular Dynamics Study.* The Journal of Physical Chemistry B, 2013. **117**(19): p. 5971-5977.
24. Xie, H.-B., et al., *Reaction Mechanism of Monoethanolamine with CO2 in Aqueous Solution from Molecular Modeling.* The Journal of Physical Chemistry A, 2010. **114**(43): p. 11844-11852.
25. Strazisar, B.R., R.R. Anderson, and C.M. White, *Degradation Pathways for Monoethanolamine in a CO2 Capture Facility.* Energy & Fuels, 2003. **17**(4): p. 1034-1039.
26. Dutcher, B., M. Fan, and A.G. Russell, *Amine-Based CO2 Capture Technology Development from the Beginning of 2013—A Review.* ACS Applied Materials & Interfaces, 2015. **7**(4): p. 2137-2148.
27. Thitakamol, B., A. Veawab, and A. Aroonwilas, *Environmental impacts of absorption-based CO2 capture unit for post-combustion treatment of flue gas from coal-fired power plant.* International Journal of Greenhouse Gas Control, 2007. **1**(3): p. 318-342.
28. Fulk, S.M. and G.T. Rochelle, *Modeling Aerosols in Amine-based CO2 Capture.* Energy Procedia, 2013. **37**: p. 1706-1719.
29. Khakharia, P., et al., *Investigation of aerosol based emission of MEA due to sulphuric acid aerosol and soot in a Post Combustion CO2 Capture process.* International Journal of Greenhouse Gas Control, 2013. **19**: p. 138-144.
30. Masiren, E.E., et al., *Effect of Temperature on Diffusivity of Monoethanolamine (MEA) on Absorption Process for CO2 Capture.* International Journal Of Engineering Technology And Sciences (IJETS) 2016. **5**(1): p. 43-51.
31. Khakharia, P., et al., *Field study of a Brownian Demister Unit to reduce aerosol based emission from a Post Combustion CO2 Capture plant.* International Journal of Greenhouse Gas Control, 2014. **28**: p. 57-64.
32. Majeed, H., et al., *Gas phase amine depletion created by aerosol formation and growth.* International Journal of Greenhouse Gas Control, 2017. **64**: p. 212-222.
33. He, Z.M., et al., *Fine Particulate Matter Concentrations in Urban Chinese Cities, 2005–2016: A Systematic Review.* International Journal of Environmental Research and Public Health, 2017. **14**(2).
34. *Aerosols & Particulate Matter*. [cited 11.01.2018]; Available from: http://www.mfg.mtu.edu/cyberman/environment/air/pmintro.html.
35. Weber, R.J., *Measurement of Particulate Matter Physical Properties*, 2012, Georgia Tech. p. 1-7.
36. Phalen, R., *The Particulate Air Pollution Controversy: A Case Study and Lessons Learned*, 2002, Kluwer Academic Publishers: Norwell, Massachusetts p. 39.
37. Kamijo, T., *Amine emission control technology of KM CDR process*, 2011: Presentation at the EPRI meeting: 'Amines for post combustion capture'.
38. van der Gjip, S., et al., *Emission reducing technologies: Aerosols*, 2012: University of Texas Conference on Carbon Capture and Storage. Austin, TX. .
39. Kolderup, H.d.S., E.; Mejdell, T.; Tobiesen, A.; Haugen, G.; Hoff, K.A.; Josefsen, K.; Strøm, T.; Furuseth, O.; Hanssen, K.F.; Wirsching, H.; Myhrvold, T.; Johnsen, K., *Emission reducing technologies*, 2011: Report H&ETQP Amine for Gassnova NF, Norway.
40. Seinfield, J.H.P., Spyros N, *Atmospheric Chemistry and Physics: From Air Pollution to Climate Change*. Third ed2016, New Jersey: John Wiley and Sons, Inc. 449.
41. Schaber, K., *Aerosol formation in absorption processes.* Chemical Engineering Science, 1995. **50**(8): p. 1347-1360.
42. Mertens, J., et al., *Understanding ethanolamine (MEA) and ammonia emissions from amine based post combustion carbon capture: Lessons learned from field tests.* International Journal of Greenhouse Gas Control, 2013. **13**: p. 72-77.
43. Grottel, S., et al., *Visual Verification and Analysis of Cluster Detection for Molecular Dynamics.* IEEE Transactions on Visualization and Computer Graphics, 2007. **13**(6): p. 1624-1631.

44. Böttinger, W., M. Maiwald, and H. Hasse, *Online NMR spectroscopic study of species distribution in MEA–H2O–CO2 and DEA–H2O–CO2.* Fluid Phase Equilibria, 2008. **263**(2): p. 131-143.
45. Han, B., et al., *Understanding CO2 Capture Mechanisms in Aqueous Monoethanolamine via First Principles Simulations.* The Journal of Physical Chemistry Letters, 2011. **2**(6): p. 522-526.
46. Hwang, G.S.S., H. M.; Paek, E.; Manogaran, D., *Reaction mechanisms of aqueous monoethanolamine with carbon dioxide: a combined quantum chemical and molecular dynamics study.* Phys Chem Chem Phys, 2015. **17**(2): p. 831-9.
47. Caplow, M., *Kinetics of carbamate formation and breakdown.* Journal of the American Chemical Society, 1968. **90**(24): p. 6795-6803.
48. Danckwerts, P.V., *The reaction of CO2 with ethanolamines.* Chemical Engineering Science, 1979. **34**(4): p. 443-446.
49. Shim, J.-G., et al., *DFT Calculations on the Role of Base in the Reaction between CO2 and Monoethanolamine.* Industrial & Engineering Chemistry Research, 2009. **48**(4): p. 2172-2178.
50. Button, J.K., et al., *Molecular dynamics simulation of hydrogen bonding in monoethanolamine.* Fluid Phase Equilibria, 1996. **116**(1): p. 320-325.
51. López-Rendón, R., et al., *Molecular Dynamics Simulations of Aqueous Solutions of Ethanolamines.* The Journal of Physical Chemistry B, 2006. **110**(30): p. 14652-14658.
52. da Silva, E.F., et al., *Molecular Dynamics Study of Ethanolamine as a Pure Liquid and in Aqueous Solution.* The Journal of Physical Chemistry B, 2007. **111**(14): p. 3695-3703.
53. Ling, Z., *Lecture 10: Homogeneous Nucleation*, 2004, University of Utah. p. 1-4.
54. Jacobson, M., *Fundamentals of Atmospheric Modeling* 2005, Cambridge University Press. p. 470.
55. Disselkamp, R. and G.E. Ewing, *Large CO2 clusters studied by infrared spectroscopy and light scattering.* The Journal of Chemical Physics, 1993. **99**(4): p. 2439-2448.
56. de Cazenove, T., et al., *Aerosol Measurement Technique: Demonstration at CO2 Technology Centre Mongstad.* Energy Procedia, 2016. **86**: p. 160-170.
57. Fujita, K., et al., *Impact of the Aerosol Particle Included in Actual Flue Gas on Amine Mist Formation/Growth in the Post-Combustion Capture Pilot Plant.* Energy Procedia, 2017. **114**: p. 930-938.
58. Khakharia, P., et al., *Predicting Aerosol Based Emissions in a Post Combustion CO2 Capture Process Using an Aspen Plus Model.* Energy Procedia, 2014. **63**: p. 911-925.
59. Khakharia, P., *Aerosol-based Emission, Solvent Degradation, and Corrosion in Post Combustion CO2 Capture.* 2015.
60. Imle, M., et al., *Predicting supersaturation by rate-based simulations of reactive absorption.* Chemical Engineering Science, 2014. **118**: p. 41-49.
61. Kraska, T., F. Römer, and A.R. Imre, *The Relation of Interface Properties and Bulk Phase Stability: Molecular Dynamics Simulations of Carbon Dioxide.* The Journal of Physical Chemistry B, 2009. **113**(14): p. 4688-4697.
62. Babarao, R. and J. Jiang, *Molecular Screening of Metal−Organic Frameworks for CO2 Storage.* Langmuir, 2008. **24**(12): p. 6270-6278.
63. Sweatman, M.B. and N. Quirke, *Modelling Gas Adsorption in Slit-Pores Using Monte Carlo Simulation.* Molecular Simulation, 2001. **27**(5-6): p. 295-321.
64. Jorgensen, W.L. and J.D. Madura, *Temperature and size dependence for Monte Carlo simulations of TIP4P water.* Molecular Physics, 1985. **56**(6): p. 1381-1392.
65. Jorgensen, W.L., et al., *Comparison of simple potential functions for simulating liquid water.* The Journal of Chemical Physics, 1983. **79**(2): p. 926-935.
66. Matsumoto, M., S. Saito, and I. Ohmine, *Molecular dynamics simulation of the ice nucleation and growth process leading to water freezing.* Nature, 2002. **416**: p. 409.

67. Oh, K.J., G.T. Gao, and X.C. Zeng, *Nucleation of Water and Methanol Droplets on Cations and Anions: The Sign Preference.* Physical Review Letters, 2001. **86**(22): p. 5080-5083.
68. Merikanto, J., H. Vehkamäki, and E. Zapadinsky, *Monte Carlo simulations of critical cluster sizes and nucleation rates of water.* The Journal of Chemical Physics, 2004. **121**(2): p. 914-924.
69. Hale, B.N. and D.J. DiMattio, *Scaling of the Nucleation Rate and a Monte Carlo Discrete Sum Approach to Water Cluster Free Energies of Formation.* The Journal of Physical Chemistry B, 2004. **108**(51): p. 19780-19785.
70. Petrov, D., et al., *A Systematic Framework for Molecular Dynamics Simulations of Protein Post-Translational Modifications.* PLOS Computational Biology, 2013. **9**(7): p. e1003154.
71. Cygan, R.T., V.N. Romanov, and E.M. Myshakin, *Molecular Simulation of Carbon Dioxide Capture by Montmorillonite Using an Accurate and Flexible Force Field.* The Journal of Physical Chemistry C, 2012. **116**(24): p. 13079-13091.
72. Ember, G., J.R. Ferron, and K. Wohl, *Self-Diffusion Coefficients of Carbon Dioxide at 1180°—1680°K.* The Journal of Chemical Physics, 1962. **37**(4): p. 891-897.
73. Stauffer, D., A. Coniglio, and D.W. Heermann, *Monte Carlo Experiment for Nucleation Rate in the Three-Dimensional Ising Model.* Physical Review Letters, 1982. **49**(18): p. 1299-1302.
74. Yasuoka, K. and M. Matsumoto, *Molecular dynamics of homogeneous nucleation in the vapor phase. I. Lennard-Jones fluid.* The Journal of Chemical Physics, 1998. **109**(19): p. 8451-8462.
75. Diemand, J., et al., *Large scale molecular dynamics simulations of homogeneous nucleation.* The Journal of Chemical Physics, 2013. **139**(7): p. 074309.
76. Sosso, G.C., et al., *Crystal Nucleation in Liquids: Open Questions and Future Challenges in Molecular Dynamics Simulations.* Chemical Reviews, 2016. **116**(12): p. 7078-7116.
77. Yasuoka, K. and M. Matsumoto, *Molecular dynamics of homogeneous nucleation in the vapor phase. II. Water.* The Journal of Chemical Physics, 1998. **109**(19): p. 8463-8470.
78. Horsch, M., et al., *Homogeneous nucleation in supersaturated vapors of methane, ethane, and carbon dioxide predicted by brute force molecular dynamics.* The Journal of Chemical Physics, 2008. **128**(16): p. 164510.

Appendices

Table A1. Force field parameters for ethanolamine and CO_2 as reported by Moosavi et al. 2015

Bond	**r_0 (Å)**	**K_r (kcal mol $^{-1}$ Å $^{-2}$)**
N-H	1.0141	868
N-C	1.4670	734
C-C	1.5211	620
C-O	1.4251	620
C-H	1.1011	680
O-H	0.9610	1106
Angle	**θ_0**	**k_θ ^{b} (kcal mol $^{-1}$ radian $^{-2}$)**
H-N-H	106.397	70
H-N-C	110.216	60
N-C-C	109.922	160
C-C-O	107.556	100
C-C-H	108.138	100
C-O-H	108.556	110
Dihedral	**A (kcal/mol)**	**F (degree)**
H-N-C-C	0.155	167.632
O-C-C-N	0.155	179.85
C-C-O-H	0.167	177.572
Intermolecular parameters	**Potential model**	**B (kcal/mol Å6)**
N-N	12-6	945.5108643
C-C	12-6	675.6122475
O-O	12-6	699.7468097
H(N)-H(N)	12-6	0.093759898
H(O)-H(O)	12-6	0
H(C)-H(C)	12-6	14.30765266

Table A2. Force field parameters for ethanolamine as reported by Da Silva et al., 2007

Bond	**r_0 (Å)**	**K_r (kcal mol $^{-1}$ Å $^{-2}$)**
N-H	1.018	394.1
N-C	1.470	320.6
C-C	4.535	303.1
C-O	1.426	314.1
C-H	1.093	335.9
O-H	0.974	369.6
angle	**θ_0**	**k_θ ^{b} (kcal mol $^{-1}$ radian $^{-2}$)**
C-O-H	108.16	47.1
H-N-H	109.5	35.0
C-C-O	109.43	67.6
C-C-H	110.07	46.4
N-C-C	110.38	66.2
H-N-C	116.78	46.0

site	R* (Å)	Є (kcal mol^{-1})	q(C)
H(O)	0.0	0.0	0.36
O	1.721	0.2104	-0.6
C(O)	1.908	0.1094	0.25
H(C)	1.387	0.0157	0.0
C(N)	1.908	0.1094	0.2
N	1.824	0.1700	-0.88
H(N)	0.6	0.0157	0.335

Table A3. Forcefield parameters for SO_2 as obtained from ATB server.

q_S	+0.652
q_O	-0.326
ε_S	1.90587
ε_O	0.4123
σ_S	0.33077
σ_O	2.6259
k_{SO}	8710000 kJ/mol Å^2
r_{OSO}	1.47 Å
k_{OSO}	6102.74 kJ/mol rad^2
$\theta_{o\,OSO}$	118.0^o

Note: R_{OSO} represents bond length between oxygen and sulfur molecules.

Table A4. Forcefield parameters for O_2 as obtained from ATB server.

q_O	0.000
ε_O	1.27911
σ_O	0.27601
k_{OO}	22843000 kJ/mol Å^2
r_{OO}	1.22 Å
$\theta_{o\,OO}$	180.0^o

Table A5. Forcefield parameters for N_2 as obtained from ATB server.

q_N	0.000
ε_N	0.43786
σ_N	0.33411
k_{NN}	61983000 kJ/mol Å^2
r_{NN}	1.10 Å

Table A6. Forcefield parameters for water (TIP4P).

q_H	0.520
q_O	0.000
q_M	-1.040
ε_H	-
ε_O	0.64852
σ_H	-
σ_O	0.31537
ε_M	-
σ_M	-
k_{HO}	502416 kJ/mol Å^2
r_{OHO}	0.9572 Å
k_{OHO}	628.02 kJ/mol rad^2
$\theta_{o\ OHO}$	104.52^o

Note: R_{OHO} represents bond length between oxygen and hydrogen molecules.

Figure A7: The number of hydrogen bonds between water and CO_2 in system IV for last 2 ns of MD run. Frames 4039-5039 represent last 2 ns of the MD run.

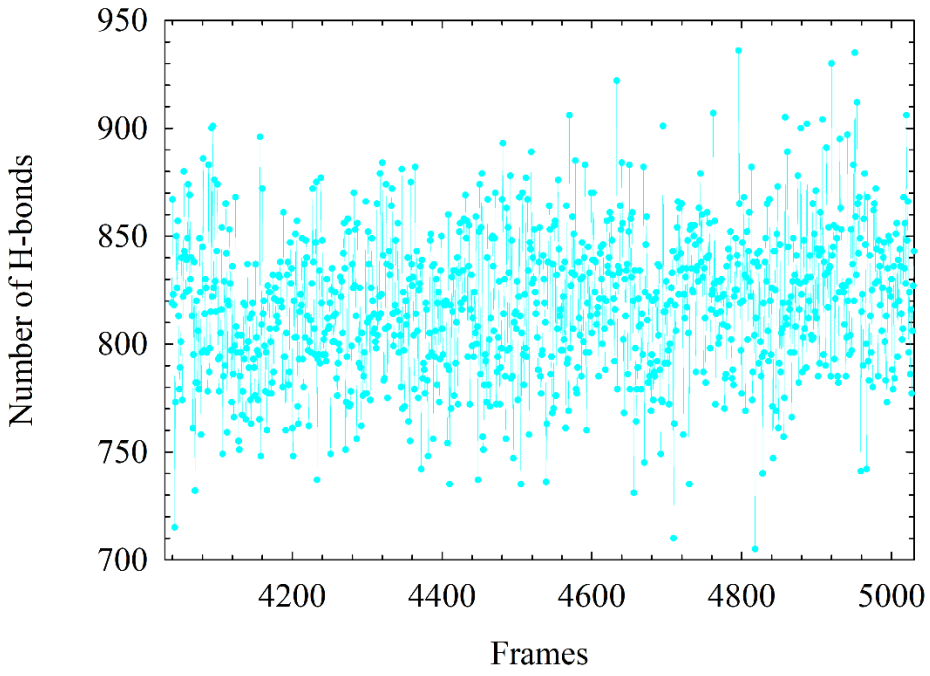

Figure A8: The number of hydrogen bonds between water and MEA in system V for last 2 ns of MD run. Frames 4106-5106 represent last 2 ns of the MD run.

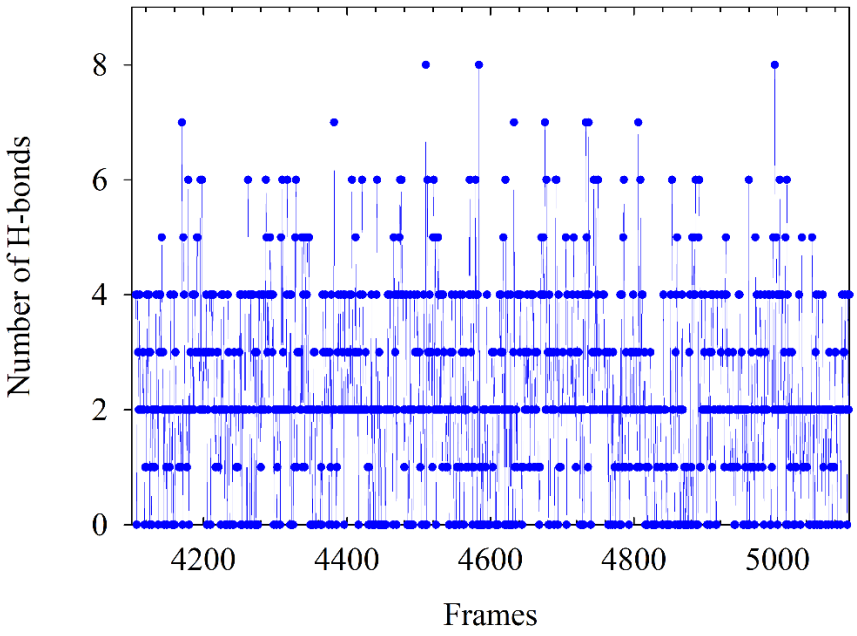

Figure A9: The number of hydrogen bonds between water and CO_2 in system V for last 2 ns of MD run. Frames 4106-5106 represent last 2 ns of the MD run.